Ground-based Infrared Profiling of Atmospheric CO_2

Beatriz Caroline Porto Ghirardi

Department of Atmospheric & Oceanic Sciences

McGill University

Montreal, Canada

June 2024

A thesis submitted to McGill University in partial fulfillment of the requirements of the degree of

Master of Science

©Beatriz Caroline Porto Ghirardi, 2024

Abstract

The increase of atmospheric CO_2 concentration has significant climate impacts, with many countries worldwide (including Canada, the United States, China, and members of the European Union) having set a net-zero emission goal for the following decades, which makes accurate measurements of its spatial and temporal variability crucial. One of the outstanding challenges is to observe the vertical distribution and variation of CO_2. Although the mean column CO_2 is useful for many climate applications, CO_2 is known to vary vertically depending on the season and time of the day, so reflecting this behavior would help reduce biases in column CO_2 products due to the vertical distribution uncertainty. Having this information would also assist in identifying emission sources (e.g., local compared to emissions from another city) and atmospheric processes controlling the atmospheric CO_2 distribution. This study examines the potential for measuring CO_2 vertical distribution and implementing innovative methods to perform profiling measurements of CO_2 using a ground-based remote sensing infrared instrument, the Atmospheric Emitted Radiance Interferometer (AERI). To verify the feasibility of CO_2 vertical profile retrieval, a simulation experiment-based assessment was conducted which replicates different instrument settings, using a Line-By-Line Radiative Transfer Model (LBLRTM) as the forward model and the Optimal Estimation as the inverse method. By evaluating key metrics of the retrieval technique, such as the Degrees of Freedom for Signal (DFS), it was verified that vertical profiling of CO_2 using AERI is possible given the expected CO_2 variability at city level and the noise level of the AERI instrument. It was also assessed that vertical levels closer to the surface are best sounded, with an accuracy of up to 5 ppmv on lower levels (from surface to around 800 m) assuming a 5% CO_2 variability every 1 km height and actual AERI's noise level. Lastly, the retrieval algorithm was applied to the real measurements of AERI acquired together with independent atmospheric sounding data in a field

campaign in order to verify the CO_2 sensing accuracies. Although issues with surface CO_2 retrieved values were identified, the algorithm was capable of improving the CO_2 vertical profile estimation from the prior information.

Résumé

L'augmentation de la concentration de CO_2 dans l'atmosphère a des répercussions importantes sur le climat. De nombreux pays (dont le Canada, les États-Unis, la Chine et les membres de l'Union européenne) ont fixé un objectif d'émissions nettes nulles pour les décennies à venir, ce qui rend cruciales les mesures précises de sa variabilité spatiale et temporelle. L'un des défis majeurs consiste à observer la distribution et la variation verticales du CO_2. Bien que le CO_2 moyen dans la colonne atmosphérique soit utile pour de nombreuses applications climatiques, on sait que le CO_2 varie verticalement en fonction de la saison et de l'heure de la journée, de sorte que la prise en compte de ce comportement contribuerait à réduire les biais dans les produits de CO_2 dans la colonne atmosphérique dus à l'incertitude de la distribution verticale. Cette information permettrait également d'identifier les sources d'émission (par exemple, les émissions locales comparées aux émissions d'une autre ville) et les processus atmosphériques qui contrôlent la distribution du CO_2 dans l'atmosphère. Cette étude examine le potentiel de mesure de la distribution verticale du CO_2 et met en œuvre des méthodes innovantes pour effectuer des mesures de profilage du CO_2 à l'aide d'un instrument de télédétection infrarouge au sol, l'Interféromètre à Rayonnement Atmosphérique (AERI en anglais). Pour vérifier la faisabilité de l'extraction du profil vertical du CO_2, une évaluation basée sur une expérience de simulation a été menée qui reproduit différents réglages de l'instrument, en utilisant un Modèle de Transfert Radiatif Ligne par Ligne (LBLRTM en anglais) comme modèle avant et l'Estimation Optimale comme méthode d'inversion. En évaluant les paramètres clés de la technique d'extraction, tels que les Degrés de Liberté du Signal (DLS), il a été vérifié qu'un profilage vertical du CO_2 à l'aide de l'AERI est possible compte tenu de la variabilité attendue du CO_2 au niveau de la ville et du niveau de bruit de l'instrument de l'AERI. Il a également été évalué que les niveaux verticaux plus proches de la surface sont les mieux sondés, avec une précision allant jusqu'à 5 ppmv aux niveaux inférieurs (de la surface à environ 800 m) en supposant une variabilité du CO_2 de 5 % tous les 1 km de hauteur et le niveau de bruit actuel de l'AERI. Enfin, l'algorithme de récupération a été appliqué aux mesures réelles de l'AERI acquises avec des données de sondage atmosphérique indépendantes lors d'une campagne sur le terrain afin de vérifier la précision de la détection du CO_2. Bien que des problèmes aient été identifiés avec les valeurs de CO_2 récupérées à la surface, l'algorithme a été capable d'améliorer l'estimation du profil vertical du CO_2 à partir des informations préalables.

Acknowledgements

First, I would like to express my gratitude to my supervisor, Prof. Yi Huang. Your insights, guidance and understanding were invaluable not only for this project, but for shaping how I will continue in my career too, and I am grateful for your support throughout my graduate studies journey. I could not have wished for a better supervisor.

I wish to thank my thesis examiner, Prof. Frédéric Fabry, for taking some time to evaluate this thesis. Your feedback is greatly appreciated.

I would also like to thank my groupmates from Professor Huang's research group for their constructive comments. In particular, a special thank you to my colleague Dr. Lei Liu for all your help in the process of this research.

I also want to express my appreciation to my family for always believing in my potential and supporting my chosen path. I would like to especially thank my sister Bruna. Your help throughout my entire academic and career journey is why I was able to pursue this degree, and I am immensely grateful for it.

Finally, I would like to acknowledge that this project has been sponsored by the Government of Canada through Environment and Climate Change Canada's "Advancing climate change science and technology" funding.

Contribution of Authors

The author, Beatriz Caroline Porto Ghirardi, was responsible for the entire writing of the thesis. Editing and feedback have been provided by the author's supervisor, Prof. Yi Huang. The study was carried out by Beatriz Caroline Porto Ghirardi, while Prof. Yi Huang provided the initial idea and supervision of the project.

The field campaign for CO_2 data acquisition carried out in February of 2024 was a joint effort of the Greenhouse Gases – Montreal Project team, in which the author also participated.

Contents

List of Figures

List of Tables

Nomenclature

A-ABL	Above Atmospheric Boundary Layer
ABL	Atmospheric Boundary Layer
AERI	Atmospheric Emitted Radiance Interferometer
B-ABL	Below Atmospheric Boundary Layer
CDFS	Cumulative Degrees of Freedom for Signal
CR	Channel Resolution
DFS	Degrees of Freedom for Signal
DLR	Downwelling Longwave Radiance
GHG	Greenhouse Gases
LBLRTM	Line-By-Line Radiative Transfer Model
OE	Optimal Estimation
pdf	Probability Density Function

1. Introduction

Global warming is considered by many to be one of the main threats to modern civilization, as human activities undoubtedly influenced the warming of the atmosphere seen over the past couple of centuries (Arias et al., 2021). Among the consequences of this rapid climate change is an increase in frequency and intensity of extreme weather events, such as heavy precipitation and droughts, leading to a rise in climate related human and vegetation mortality (Pörtner et al., 2022). The changes caused by man-induced global warming also increases damages to key economic sectors, with these negative impacts being more noticeable for economically vulnerable groups (Pörtner et al., 2022).

Earth's surface absorbs solar radiation, also called shortwave radiation due to its main composition being of smaller wavelengths, and then emits part of this energy back in the form of longwave radiation (Liou, 2002). In the atmosphere, a few trace gases, such as H_2O, CO_2, O_3 and CH_4, absorb part of the energy being emitted by Earth, causing the surface of the planet to be 30°C warmer than it would be otherwise (Houghton, 2001). This is called the greenhouse effect and is what allows our planet to have a hospitable average temperature for humans. The trace gases responsible for this phenomenon are known as greenhouse gases (GHG).

However, the increase in anthropogenic GHG emissions since the Industrial Revolution intensified the greenhouse effect (Mitchell, 1989). CO_2 is considered to be the primary human emitted greenhouse gas, with a total of around 40 billion tonnes of CO_2 have been released into the atmosphere as of 2019 (Canadell et al., 2021, pp. 773). This, alongside the already emitted other GHG and current emission trends, means that a global warming of at least 1.5 °C will likely occur in the 21st century (Allen et al., 2018, pp. 81).

This widespread warming causes changes in other physical and chemical variables that also help regulate temperature on Earth, with these alterations themselves amplifying or diminishing global warming. These mechanisms are called "climate feedback", with positive ones intensifying the warming effects of GHG emissions, and negative ones doing the opposite (Colman & Soden, 2021). A great concern of CO_2 emissions is its enhancement of the water vapor feedback, a positive climate feedback where the warming climate causes a greater release of water vapor in the atmosphere which, in return, increases the temperature even more (Colman & Soden, 2021), with its considerable strength making more difficult to slow down the warming process (Arias et al., 2021).

Because of global warming multiple negative impacts, many countries, including Canada, the United States, China, and members of the European Union, made commitments to achieve net-zero carbon emission by 2050 (United Nations, n.d.), in a collective effort to mitigate climate change. To achieve this goal, mapping of direct and indirect carbon emissions will play an essential role in monitoring progress and supporting carbon policies (Chen et al., 2022), as such, technologies to accurately measure atmospheric CO_2 will be indispensable.

Moreover, a deep understanding of the carbon cycle is vital for climate model predictions, since uncertainties in this variable leads to uncertainties in how the models shape their responses (Arora et al., 2020). Accurate CO_2 measurements, especially related to its daily and seasonal cycles, is essential to extend the necessary knowledge for trustworthy climate models. Improvements in satellite CO_2 measurements over the past decade have greatly contributed to a global understanding of CO_2 patterns (Imasu et al., 2023), but their performance for near-surface values is not sufficiently precise (Wunch et al., 2017). In-situ instruments also allowed for high precision in CO_2 quantification (Xia et al., 2022), but the altitude and frequency of these measurements may not be enough to fully capture the CO_2 cycle in the lower troposphere.

Ground-based remote sensing instruments presents as a great tool to validate satellite-based instruments and to provide frequent CO_2 measurements in the troposphere (Wunch et al., 2011). The main network of instruments being used for this purpose is the solar absorption spectrometers of The Total Carbon Column Observing Network, or TCCON (Wunch et al., 2011). However, these instruments can only measure CO_2 when sunlight is available, which misses the night portion of CO_2 daily cycle (Ghadikolaei, 2017). As such, there is a need for a ground-based instrument capable of capturing CO_2 concentration during the whole day to fill this gap.

One potential option for this purpose is the Atmospheric Emitted Radiance Interferometer (AERI), a Fourier transform spectrometer that measures downwelling longwave radiance (DLR) (Demirgian & Dedecker, 2005). Because AERI measures the radiation emitted by Earth's atmosphere in the mid and far-infrared range, this permits the use of CO_2 absorption bands in this spectral region to estimate atmospheric CO_2 throughout the whole day. Although some research has been done in analyzing AERI's potential for CO_2 retrieval (Ghadikolaei, 2017), there is still a lack of full understanding of its capabilities, especially in North America.

The main objective of this work is to evaluate AERI's capability of retrieving the vertical profile of CO_2. The study starts with the use of synthetic DLR spectra simulating AERI's measurements and idealized background atmospheric knowledge to understand the theoretical potential of CO_2 profile retrieval by AERI. These synthetic experiments are designed to assess both the necessary instrument requirements and the different profile shapes that can be captured. Next, the retrieval is applied to real AERI radiance spectra and validated against CO_2 measurements made by in-situ instruments to test its capability under real atmospheric conditions.

2. Literature review

2.1 Atmospheric CO_2 vertical distribution

Carbon does not have a singular sink, and instead flows between Earth's subsystems in a process called the global carbon cycle (Prentice et al., 2001, pp. 191). When considering only the terrestrial carbon cycle, CO_2 concentration is known to vary vertically both in daily and seasonal terms, due to its interactions with the biosphere, different anthropogenic source patterns throughout the year, and atmospheric physical processes (Biraud et al., 2013; Li et al., 2014; Park et al., 2021; Bezyk et al., 2023).

Photosynthetic activity influences CO_2 vertical profile because it represents a sink of atmospheric CO_2. During the summer months, average CO_2 concentrations is typically lower near surface and increases with height due to higher plant activity and reduced anthropogenic emissions associated with heating, while the opposite is observed in the winter, where a smaller presence of plants combined with increased anthropogenic emissions creates CO_2 profiles with greater concentrations near the ground (Biraud et al., 2013; Cheng et al., 2018; Xia et al., 2022).

Anthropogenic emissions not only influence the total column CO_2 concentration, which is an already well-established knowledge when it comes to global warming discussions (Arias et al., 2021), but also the vertical distribution of said concentrations. Many studies have attributed peaks in CO_2 to different human emitted sources, such as heating during winter (Cheng et al., 2018; Mitchell et al., 2018; Venturi et al., 2020), and combustion of fossil fuels, especially during rush hours (Xia et al., 2022; Bezyk et al., 2023).

The anthropogenic contribution is even more pronounced in urban regions. While CO_2 concentrations in areas outside of urban zones can be more influenced by photosynthetic activity and respiration, the pronounced peaks in CO_2 concentration often seen in urban environments is attributed to anthropogenic emissions (Lu et al., 2018; Wu et al, 2023). Anthropogenic CO_2 is seen in multiple environments, including rural (Hu et al, 2018), however, the higher levels of energy consumption, use of transport that utilizes fossil fuels, and presence of industries in urban regions significantly contribute to its higher CO_2 emissions (Crippa et al, 2021).

The atmospheric conditions also greatly influence the vertical distribution of CO_2. The height of the atmospheric boundary layer (ABL), which is defined as the lower portion of the troposphere that is strongly influenced by exchanges with the earth's surface (Markowski & Richardson, 2010), has been associated with peaks and lows of CO_2 concentration in its daily cycle (Park et al., 2022).

At the beginning of the morning, before the sunrise, the ABL tends to be its shallowest due to temperature inversions caused by radiation cooling from the surface. As solar radiation warms the surface, this temperature inversion is broken, allowing for air to rise more easily, and extending the height of the ABL, which usually peaks in the afternoon (Chen et al., 2024). Because vertical air mixing is greater within the ABL, CO_2 concentration tends to be more evenly distributed (thus overall lower) across different heights during the afternoon and beginning of evening hours, while stronger CO_2 peaks near the surface often occur from late night to early morning (Li et al., 2014; Xia et al., 2022).

With these factors in mind, accurate measurements of CO_2 vertical distribution are essential to capture such daily and seasonal variations at distinct locations. Multiple measuring techniques and instruments can be used for CO_2 profiling, and understanding the benefits and limitations of the major techniques can help on properly applying them to improve new methods and achieve higher accuracy in CO_2 estimation.

2.2 Atmospheric CO_2 measuring instruments

The types of measurements used in CO_2 vertical profiling can be divided in three groups: in-situ, satellite-based, and ground-based measurements, and each has its own set of advantages and drawbacks, which are presented over the next three subsections.

2.2.1 In-situ measurements

In-situ measurements includes instruments placed at surface level, allocated in towers, and mounted in aircrafts, which allows for local quantification of CO_2 concentration. Tower measurements allow for long-term record of CO_2 in multiple levels within the boundary layer, permitting insights into the daily and seasonal CO_2 cycles with a reasonable time frequency (Cheng et al., 2018; Shan et al., 2022), as well as more long-term trends in CO_2 concentration, such as the known CO_2 keeling curve produced with data from the Mauna Loa observatory in Hawaii (Keeling et al., 1976). However, the vertical range in which CO_2 measurements are possible is limited to the height of the tower, meaning that other techniques are required to measure higher altitudes directly.

Gas analyzing instruments mounted in aircrafts are often used for this goal (Biraud et al., 2013, Xia et al., 2022). Since aircrafts are able to reach greater heights, this allows for the investigation of CO_2 profiles in relation to the ABL behavior throughout the day, as well as more in-depth insight into atmospheric CO_2 cycles when it comes to factors less influenced by the surface, such as emissions from other locations (Xia et al., 2022). Because they directly measure the CO_2 in the region of interest, they are applied as validation values for remote sensing estimation techniques (Yang et al., 2020). A drawback of this type of data acquisition is its low temporal resolution due to the frequency of flights being small when compared to other approaches.

2.2.2 Satellite-based instruments

Measurements from spaceborne instruments have been used for estimating different greenhouse gases for a few decades, such as the use of the Atmospheric Infrared Sounder (AIRS), an instrument on board of the National Aeronautics and Space Administration (NASA) Aqua satellite, for atmospheric CO_2 retrieval (Engelen et al., 2004). AIRS is an infrared spectrometer with 2378 channels covering the 650 – 2675 cm^{-1} spectral region (Engelen et al., 2004). Although the instrument was not designed for the purpose of CO_2 estimations, the strong 15 μm CO_2 absorption band showed good potential for doing so (Crevoisier et al., 2003), which culminated in the retrieval of a global mid-troposphere monthly mean CO_2 concentration with 15° x 15° spatial resolution (Crevoisier et al., 2004).

The first mission focused on measuring greenhouse gases from space came with the Greenhouse gases Observing SATellite (GOSAT, or IBUKI in Japanese), a collaborative effort from three Japanese institutions: the Japan Aerospace Exploration Agency (JAXA), the National Institute for Environmental Science, and the Ministry of the Environment, and it was launched in 2009 (Kuze et al., 2009).

The instrument responsible for capturing the data required to estimate column-averaged CO_2 (XCO_2) is the Thermal And Near infrared Sensor for carbon Observation – Fourier Transform Spectrometer (TANSO-FTS). TANSO-FTS measures reflected sunlight radiance during daytime in the infrared spectral region, which includes the strong 2.0 μm and weak 1.6 μm CO_2 absorption bands. The instrument also collects observations using thermal infrared during both daytime and nighttime modes (JAXA, 2011). Ever since GOSAT's launch, a few other satellite-based instruments for CO_2 quantification have been instituted, such as the Orbiting Carbon Observatory-2 (OCO-2) from NASA in 2014 (Crisp et al., 2017), and the Chinese Global Carbon Dioxide

Monitoring Scientific Experimental Satellite (TanSat) by the Ministry of Science and Technology of China in 2016 (Liu et al., 2018).

The main advantage of spaceborne instruments is its spacial coverage, which allows for global analysis of CO_2 emissions (Hu et al., 2024). Studies have used these products to show the correlation of anthropogenic CO_2 in urban environments with other gases enhancements (Park et al., 2021), the impact of city's subways implementation in CO_2 emissions (Dasgupta et al., 2023), and overall trends in global CO_2 emissions (Dou et al., 2023).

A significant drawback of satellite-based devices is its difficulty with estimating lower troposphere and near surface CO_2 values, which is also the region where we tend to see most of CO_2 vertical variation (O'Dell et al., 2012, Wunch et al., 2017). Moreover, the direct product of most satellites dedicated to GHG measurements is total column CO_2 (Yang et al., 2020), so techniques to retrieve the CO_2 vertical profile continue to be developed, including methods that utilize machine learning (Xie et al., 2023).

2.2.3 Ground-based instruments

A primary way to obtain a more detailed quantification of CO_2 surface emissions when compared to satellite-based data, as well as validate satellite GHG products, is with the use of ground-based instruments. Their bottom-up view of the atmosphere and known fixed location, alongside a more frequent data acquisition than many in-situ measurements, allows for ground-based devices to be a great validation mechanism for satellites GHG quantifications (Yang et al., 2020; Karbasi et al., 2022; Imasu et al. 2023).

One of the main ground-based instruments networks currently used is The Total Carbon Column Observing Network (TCCON), which was established in 2004 (Wunch et al., 2011).

TCCON is composed of ground-based Fourier transform spectrometers that retrieves column-averaged values of multiple greenhouse gases (including XCO_2) from the near-infrared solar absorption spectra (Wunch et al., 2011). The main objectives of the network are to provide primary validation datasets of XCO_2 (and XCH_4) to spaceborne instruments, contribute to knowledge of the carbon cycle worldwide, and be a bridge between satellite-based and in-situ measurements (Wunch et al., 2011). TCCON spectrometers have two detectors that cover the spectral region from 3900-15500 cm^{-1} with approximately 0.02 cm^{-1} spectral resolution, which includes the coverage of multiple satellites, and allows for a precision of less than 1 ppm in the XCO_2 retrieval (Wunch et al., 2011).

Data from TCCON have been used to estimate CO_2 fossil fuel city emissions (Babenhauserheide et al., 2020), overall emissions in metropolitan areas (Ohyama et al., 2023), and local and regional CO_2 enhancements from different sources (Mottungan et al., 2024). Moreover, TCCON instruments shows potential to retrieve the vertical profile of CO_2 (Roche et al., 2021), with distinct retrieval techniques being applied for this purpose (Parker et al., 2023).

However, because TCCON spectrometers use solar absorption spectra, only daytime CO_2 retrieval is possible (Babenhauserheide et al., 2020), which does not allow for the capture of the full daily cycle of CO_2 (Ghadikolaei, 2017). As such, ground-based instruments that can be utilized to estimate CO_2 concentration during both day and night hours are necessary to fill this gap.

Fourier-transform spectrometers with spectral coverage on the thermal-infrared are a great option for this purpose, since this spectral range is emitted by Earth's atmosphere throughout the whole day (Liou, 2002). The Atmospheric Emitted Radiance Interferometer (AERI), which will be described in detail in section 3.4, presents as a potential complement for ground-based measurements of CO_2, which is one of the motivations of this thesis.

AERI has been used to retrieve temperature and water vapor profiles for many years (Feltz et al., 1998; Lewis et al., 2020; Smith et al., 2021; Huang et al., 2023) and have shown potential to retrieve other atmospheric variables, such as Aerosol Optical Depth (Seo et al., 2022). The ability of AERI retrieving CO_2 also has been demonstrated (Ghadikolaei, 2017). However, research in more locations, with different characteristics and distinct climates, is still needed to fully understand its retrieval capacity.

3. Methodology

3.1 The Retrieval Technique

The retrieval technique applied in this study can be divided into two sections: the application of a forward model, and the use of an inverse method.

A forward model describes the physics of the measurement process (Rodgers, 2000), meaning that given an atmospheric state to be retrieved (e.g., temperature profile, water vapor and trace gases concentration profiles, etc.), the forward model maps this state vector from state space to measurement space. However, the representation of the physical processes to obtain the measurement is often limited, requiring an approximation of reality and, thus, will have errors. As such, the relationship between measurement and atmospheric state can be represented as:

$$\boldsymbol{y} = \boldsymbol{F}(\boldsymbol{x}, \boldsymbol{b}) + \boldsymbol{\varepsilon} \tag{1}$$

where **y** is the measurement vector, **F** is the forward model applied on state vector **x** alongside model parameter **b**, which represents other atmospheric variables that influences the measuring procedure but are considered to be known, and $\boldsymbol{\varepsilon}$ encompasses the measurement error and the inherent imperfection of the forward model on its description of the physics for the measuring process. In this project, the **x** vector represents the CO_2 vertical profiles to be retrieved.

Often in inverse problems, **F(x)** can be considered linear when it comes to its error analysis. Linearizing Equation 1 at a reference state $\mathbf{x_0}$, we have:

$$\boldsymbol{y} = \boldsymbol{F}(\boldsymbol{x_0}) + \frac{\boldsymbol{\delta F}(\boldsymbol{x})}{\boldsymbol{\delta x}}(\boldsymbol{x} - \boldsymbol{x_0}) + \boldsymbol{\varepsilon} = \boldsymbol{F}(\boldsymbol{x_0}) + \boldsymbol{K}(\boldsymbol{x} - \boldsymbol{x_0}) + \boldsymbol{\varepsilon} \tag{2}$$

in which **K** is the Jacobian matrix and represents the sensitivity of the forward model to the atmospheric state.

The inverse method is the technique utilized to obtain an estimation of the atmospheric state based on the measurements made. The inverse method applied in this study is the Optimal Estimation (OE) method, as described in Rodgers (2000).

The OE method is based on the Bayes' theorem, which defines the probability of an event while taking into account a prior knowledge that influences said event. For atmospheric retrieval, this prior information comes from the atmospheric state of interest (represented as $\mathbf{x_a}$), which can be the climatology of $\mathbf{x}$. The probability density function (*pdf*) of the atmospheric state of interest $\mathbf{x}$ given a measurement $\mathbf{y}$, the $\mathbf{P(x|y)}$, will be:

$$\boldsymbol{P(x|y) = \frac{P(y|x) \cdot P(x)}{P(y)}} \tag{3}$$

where $\mathbf{P(y|x)}$ is the *pdf* of a measurement given a certain atmospheric state, $\mathbf{P(x)}$ is the *pdf* of the prior information of the atmospheric state, and $\mathbf{P(y)}$ is interpreted as the prior information of the measurement, although in practice it only works as a normalizing factor and can be omitted (Rodgers, 2000).

Due to its well representation of many physical processes and for being uncomplicated to manipulate algebraically, a Gaussian distribution can be applied to the *pdf*'s of Equation 3, resulting in:

$$\boldsymbol{-2 \ln P(x|y) = (y - Kx)^T S_\varepsilon^{-1} (y - Kx) + (x - x_a)^T S_a^{-1} (x - x_a) + c} \tag{4}$$

where $\mathbf{S_\varepsilon}$ and $\mathbf{S_a}$ represents the measurement error covariance matrix and the a priori covariance matrix, respectively, and $\mathbf{K}$ is the Jacobian. For the applications of this study, $\mathbf{S_\varepsilon}$ describes the covariance of measurement error on different channels of AERI, while $\mathbf{S_a}$ expresses the covariance of different atmospheric state vertical layers. The diagonal components of a covariance matrix represent the variance of each said component, while the off-diagonal elements are the covariance between these elements. The Jacobian is defined as $\boldsymbol{K} = \nabla_x F$, and represents the sensitivity of the forward model to the true state of the atmosphere **x**.

The most probable state of **x** will be, therefore, the one that optimizes the *a posteriori* error by approximating the derivative of Equation 4 to zero (Rodgers, 2000). By applying the Gauss-Newton iteration method, we get that each time step will be:

$$\boldsymbol{x_{i+1}} = \boldsymbol{x_i} + \left(\boldsymbol{S_a^{-1}} + \boldsymbol{K_i^T} \boldsymbol{S_\epsilon^{-1}} \boldsymbol{K_i}\right)^{-1} \boldsymbol{K_i^T} \boldsymbol{S_\epsilon^{-1}} \left[\boldsymbol{y} - \boldsymbol{F}(\boldsymbol{x_i}) + \boldsymbol{K}(\boldsymbol{x_i} - \boldsymbol{x_a})\right] \tag{5}$$

where *i* symbolizes each iteration step.

Since the calculation of the Jacobian matrix is the most computationally expensive part, and that its values tend to have a smaller variation after each iteration, **K** is calculated up until the third iteration step. The retrieval is considered to be converged once the radiance change in all channels from one iteration step compared to the previous one is less than 10^{-6} W/(m^2·sr·cm^{-1}), which is around 0.001% of the average radiance in the 15 μm CO_2 absorption band. For all the experiments, this criterion was met within the first 5 iterations.

3.2 Information Content and Error Analysis

When it comes to evaluating the retrieval, two variables stand out: the Averaging Kernel matrix and the Degrees of Freedom for Signal.

The Averaging Kernel (**A**) is defined as $\boldsymbol{A} = (S_a^{-1} + K_i^T S_\epsilon^{-1} K_i)^{-1} K_i^T S_\epsilon^{-1} K$, and shows the sensitivity of the retrieval to the true atmospheric state. With this matrix **A**, we are able to see where most of the retrieval information for each atmospheric level comes from. An averaging kernel value of 1 for a certain atmospheric level means that all the retrieval information for that level comes from itself, being independent from all the other levels. However, this ideal situation is not what happens, and adjacent atmospheric levels influence each other's estimates, making the averaging kernel value less than 1.

The Degrees of Freedom for Signal (DFS) is defined as $DFS = tr(\boldsymbol{A})$ and equates to how many independent pieces of information we can get from the retrieval, meaning that the higher the DFS value, the higher is the information content of the retrieval. Ideally, each vertical level would be independent from the other ones (DFS = 1 for each level), but that is usually not the case. When getting the total DFS of the atmosphere, it is important for DFS > 1, so that we can have a vertical profile of the variable of interest (CO_2).

To analyse the error of the retrieval, the Root Mean Squared Error (RMSE) between the true and retrieved CO_2 profiles is determined. The RMSE at each level is calculated as:

$$\boldsymbol{RMSE} = \sqrt{\sum_{i=1}^{n} \frac{(\hat{\boldsymbol{x}}_i - \boldsymbol{x}_i)^2}{\boldsymbol{n}}} \tag{6}$$

where $\hat{x}_i$ is the retrieved value for simulation i, x_i is the true value, and n is the number of simulations.

The posterior uncertainty covariance matrix of the retrieval is calculated as shown in Equation 7 and should represent a smaller quantity than the prior uncertainty ($\mathbf{S_a}$ matrix) in order for the retrieval to be considered effective (Rodgers, 2000).

$$\boldsymbol{S} = \left(\boldsymbol{K}_i^T\, \boldsymbol{S}_\epsilon^{-1}\, \boldsymbol{K}_i + \boldsymbol{S}_a^{-1}\right)^{-1} \tag{7}$$

3.3 Radiative Transfer and LBLRTM Algorithm

The principal that makes the retrieval of CO_2 from infrared radiation measurements possible is the Radiative Transfer theory, which can explain how electromagnetic radiation interacts with atmospheric gases. The explanation of the theory, as well as how to get the Radiative Transfer Equation was mainly based on the work of Liou (2002).

The radiation intensity may change due to absorption or scattering by different matter on a medium. This interaction is characterized by the mass extinction cross section, which is defined as:

$$\boldsymbol{k_e = k_s + k_a} \tag{8}$$

where $\boldsymbol{k_s}$ is the mass scattering cross section and $\boldsymbol{k_a}$ is the mass absorption cross section, and they depend on the wavelength λ being evaluated. For a non-scattering atmosphere, which is a good approximation for clear-sky in the thermal infrared region (Ghadikolaei, 2017)20172017 and the case for this study, $\boldsymbol{k_s}$ is negligible, meaning that $\boldsymbol{k_e \approx k_a}$.

As such, when light of a specific wavelength λ and intensity I_λ passes through a medium, its attenuation along a path $\boldsymbol{ds}$ can be described as:

$$\boldsymbol{dI_\lambda = -k_a\, \rho\, I_\lambda\, ds} \tag{9}$$

where $\boldsymbol{\rho}$ represents the density of each trace gas in the medium.

Integrating Equation 9 between a start point $\boldsymbol{s_1}$ and end point $\boldsymbol{s_2}$, and assuming that the path is homogeneous, we get:

$$\boldsymbol{I_\lambda(s_2) = I_\lambda(s_1) \exp\left[-\int_{s_1}^{s_2} \rho(s)\, k_a\, ds\right]} \tag{10}$$

The term in brackets (without the minus sign) is called optical path, and when $\boldsymbol{s_1}$ and $\boldsymbol{s_2}$ are vertical coordinates, is also called optical depth or optical thickness τ. From τ, we can derive the transmittance, which is defined as:

$$\boldsymbol{t = e^{-\tau}} \tag{11}$$

From Kirchhoff's Law, we know that at thermal equilibrium, the radiation absorption by a medium equals its emission. As such, we can write:

$$\boldsymbol{dI_{abs} = -k_a\, \rho\, I_\lambda\, ds = -dI_{em} = -k_a\, \rho\, B_\lambda(T)\, ds} \qquad (12)$$

where **$B_\lambda(T)$** represents the Planck function for wavelength **λ** and temperature **T**.

With this, we can write the basic form of the Radiative Transfer Equation as:

$$\boldsymbol{dI_\lambda = dI_{abs,\lambda} + dI_{em,\lambda} \rightarrow \frac{dI_\lambda}{ds} = k_a\, \rho\, (B_\lambda(T) - I_\lambda)} \qquad (13)$$

From Equation 13, it is possible to derive the upward and downward portions of atmospheric radiation, with the downward component being:

$$\boldsymbol{I_\lambda{}^{\downarrow}(\tau, -\mu) = \int_0^\tau B_\lambda\big(T(\tau')\big)\, e^{-\frac{(\tau-\tau')}{\mu}} \frac{d\tau'}{\mu}} \qquad (14)$$

where $\mu = \cos(\theta)$, with θ being the zenith angle. Note that the optical depth **τ** is used as the vertical coordinate.

Another important factor in radiative transfer is the weighting function, which represents how much absorption occurs at a given point in relation to the total absorption, and can be written as:

$$\boldsymbol{W(z) = \frac{k_a\, \rho\, (z)}{\mu}\, t(z)} \qquad (15)$$

For downwelling radiation, the weighting function is largest at the surface. We can now write Equation 14 in terms of the weighting function (and wavenumber ν):

$$\boldsymbol{I_\nu{}^{\downarrow} = \int_0^\infty B_\nu\big(T(z')\big)\, W_\nu(z', z)\, dz} \qquad (16)$$

Equation 16 is the main form of the Radiative Transfer Equation for downwelling radiation, and for it to be as close to "exact" as possible, the transmittance **$t(z)$** needs to account for the absorption of all known gases for wavenumber **ν** at altitude **z**, meaning:

$$\boldsymbol{k_{a,v}} \cdot \boldsymbol{\rho(z)} = \sum_{i=1}^{N} \boldsymbol{k_{a,i}(z)\rho_i(z)} \tag{17}$$

where **N** is the number of gases. This is the called line-by-line calculation.

In this project, the Line-By-Line Radiative Transfer Model (LBLRTM) was used (Clough et al., 1992). The LBLRTM calculates the monochromatic radiative transfer with high accuracy and is capable of simulating both upwelling and downwelling radiance (Clough et al., 2014). The input of the model is an atmospheric profile that includes temperature, humidity, and concentration of many trace gases, such as CO_2, O_3, and CH_4. In order to calculate the mass absorption cross section ($\boldsymbol{k_a}$) of each gas, LBLRTM mainly uses the shape, width and position information of the absorption lines (and absorption continuums) provided by the HIgh-resolution TRANsmission molecular absorption (HITRAN) database. LBLRTM then calculates the optical depth and uses it to compute the radiance spectra by applying a discrete version of the radiative transfer equation.

3.4 AERI Instrument

The Atmospheric Emitted Radiance Interferometer, or AERI (Figure 1), is a ground-based Fourier transform spectrometer that measures downwelling longwave radiance emitted by Earth's atmosphere (Demirgian & Dedecker, 2005). It was developed by the University of Wisconsin Space Science and Engineering Center in 1992, supported by the Atmospheric Radiation Measurements (ARM) program of the United States Department of Energy (Knuteson et al., 2004a), with the first operational AERI being deployed in 1995. The following information, which explains the instrument specifications and operation, was taken from Knuteson et al. (2004a) and Knuteson et al. (2004b), unless stated otherwise.

Figure 1. AERI instrument located at the top of Burnside Hall building, McGill University downtown campus.

AERI measures downwelling atmospheric emitted radiance from 3.3 μm (3020 cm^{-1}) to 19 μm (520 cm^{-1}), encompassing both middle and far-infrared regions. AERI is a zenith viewing instrument, with a field-of-view (FOV) of 2.6 degrees, a (unapodized) spectral resolution of 0.5 cm^{-1}, and a temporal resolution of 20 seconds in rapid sampling mode and 8 minutes in normal sampling mode.

AERI can be divided in to two major sets: the optics bench assembly and the electronics support equipment. The main components of the optics bench assembly are an interferometer, two blackbodies and two detectors, one that is responsible for the longwave infrared measurements, and one for the shortwave infrared region, with the longwave cut-off being at about 1800 cm^{-1}. Regarding the blackbodies, they are used to calibrate the measured spectra, with one operating at near outdoor ambient temperature (called Ambient Blackbody, or ABB), and one that functions at a fixed controlled temperature around 60°C (called Hot Blackbody, or HBB).

The major parts of the electronics support equipment are the housekeeping system, the scene mirror controller, the blackbody controller, and the control computer. The housekeeping system collects temperature and voltage data across multiple components of AERI every 5 seconds to ensure good instrument performance. The scene mirror controller applies employing microstepping positioning to achieve an accuracy of ± 5 arc s, and ensure that the scene mirrors are in a safe position in case of precipitation or overtemperature. The blackbody temperature controller regulates the HBB temperature, maintaining at a narrow range around the reference temperature. The control computer is used to regulate multiple systems inside AERI, including obtaining interferometer and housekeeping data, evaluating its performance, and transferring raw data to the front-end processor.

The radiance data is acquired through the use of an interferometer. The atmospheric radiance that will reach the interferometer is initially divided in two light beams by a beam-splitter, with one going to a fixed mirror and the other to a moving mirror. The beams are reflected by the mirrors and, when combined, the difference in their paths cause a wave interference pattern, called interferogram (Ghadikolaei, 2017). A Fourier transform algorithm is then applied to convert the interferogram signal into calibrated radiance spectra. AERI's calibration includes correction for nonlinearities in the longwave band, radiometric calibration using the reference hot and ambient blackbodies, and spectral line shape effects correction.

3.5 Synthetic Experiment Setting

First, the retrieval algorithm is tested using synthetic radiance data obtained from LBLRTM. For this (and later for the retrieval), we first need to define a prior atmospheric profile, as well as the content of the matrices $\mathbf{S_a}$ and $\mathbf{S_\varepsilon}$.

The prior profile is obtained from the fifth generation European Centre for Medium-Range Weather Forecasts atmospheric reanalysis dataset, ERA5 (Hersbach et al., 2020). A 6-hourly mean ERA5 dataset from 2012 to 2022 within a grid-box encompassing the city of Montréal is used. The

ERA5 atmospheric variables utilized (geopotential, pressure, temperature, specific humidity, and ozone mass mixing ratio) all come from the "hourly data on pressure levels from 1940 to present" dataset. The CO_2 profile shape and concentration values are determined according to the intention of each experiment.

When it comes to the variability of CO_2 concentration, literature shows that CO_2 can vary more than 45 ppm near the surface and then decreases with height, reaching less than 5 ppm at around 200 hPa (O'Dell et al., 2012). The resolution of the vertical profile is set to be 100 m for the first 5 km altitude, and then the layer thickness increases by 10% for higher levels. For simplicity, $\mathbf{S_a}$ is set to have a 5% CO_2 concentration variability for every 1 km layer thickness. This variability is proportionally adjusted to account for the changing vertical resolution under the assumption that a square root relation characterizes the random errors. Is also important to note that more in-situ measurements would be required in future work to understand better the variability of CO_2 with altitude, especially when it comes to differences between urban and rural environments. All off-diagonal elements of $\mathbf{S_a}$ are set to zero.

For the $\mathbf{S_\varepsilon}$ matrix, its diagonal values are set to be the average noise of AERI for each of its channels, and the off-diagonal values are set to zero (meaning no correlation between channels). For the synthetic experiments, all other atmospheric variables (e.g., temperature, water vapor, etc.) are assumed to be perfectly known and there is no assigned correlation between variables.

To test different components of the retrieval, we set 8 distinct cases to simulate possible scenarios, all using a constant CO_2 vertical profile of 420 ppmv for the prior and random profiles with concentrations varying between 350 ppmv to 470 ppmv for the true state. These random profiles are normally distributed around the prior 420 ppmv as to make most profiles to fall within the assigned CO_2 variability. The summary of the cases is shown in Table 1.

Case 1 is the ideal scenario, where the channel resolution (CR) is set to 0.1 cm^{-1} wavenumber (finer than the actual AERI), and the noise is reduced by half. Case 2 represents an improved instrument, where the CR is also set to 0.1 cm^{-1}, but the noise stays the same as AERI's actual noise. Case 3 exemplifies a faulty instrument, where the CR is the real AERI resolution of 0.5 cm^{-1}, but its noise is triple of the average real noise. Case 4 is an optimal real instrument, where CR = 0.5 cm^{-1}, but the noise is half of AERI's actual noise.

Case 5 is the real scenario, so CR = 0.5 cm^{-1} and the noise is AERI's real noise. Case 6 uses only channels around the 15 μm CO_2 absorption band (between 624 and 712 cm^{-1}) for the retrieval. Case 7 uses a summer prior profile (average ERA5 10 years climatology for July, August, and September months), and Case 8 uses a winter prior profile (average ERA5 10 years climatology for January, February, and March months).

Table 1. Distinct real and hypothetical instrument simulations description.

Case Number	Channel Resolution	Number of Channels	Noise Level	Background
1	0.1 cm^{-1}	12792	0.5x S_e	ERA5 – all year
2	0.1 cm^{-1}	12792	1x S_e	ERA5 – all year
3	0.5 cm^{-1}	2650	3x S_e	ERA5 – all year
4	0.5 cm^{-1}	2650	0.5x S_e	ERA5 – all year
5	0.5 cm^{-1}	2650	1x S_e	ERA5 – all year
6	0.5 cm^{-1}	179	1x S_e	ERA5 – all year
7	0.5 cm^{-1}	2650	1x S_e	ERA5 – Summer
8	0.5 cm^{-1}	2650	1x S_e	ERA5 – Winter

Moreover, to see if the retrieval is capable of distinguishing distinct vertical CO_2 profiles, we test different combinations of prior and true CO_2 profile shapes, including a vertically constant profile, a decreasing and increasing CO_2 concentration with height profiles to simulate possible conditions typically seen in winter and summer, and bell-shaped profiles to simulate plumes of CO_2.

For the increasing and decreasing shapes, the CO_2 profile follow the equation described by Ghadikolaei (2017), which is also exhibited below.

$$\boldsymbol{CO_2(z) = a_2 \cdot \exp(a_1 \cdot z) + a_0} \tag{18}$$

where $\boldsymbol{CO_2(z)}$ represents the CO_2 concentration at altitude $\boldsymbol{z}$, $\boldsymbol{a_0}$ equates to the CO_2 value at high enough altitudes, $\boldsymbol{a_1}$ controls the curvature of the profile, and $\boldsymbol{a_2}$ specifies the concentration of CO_2 at z = 0. A positive $\boldsymbol{a_2}$ value means that the CO_2 concentration will decrease with height. As recommended by Ghadikolaei (2017), $\boldsymbol{a_1}$ ranges between -0.5 and -7 in order to have realistic CO_2 values in the profile.

As for the bell-shaped profile, the CO_2 vertical distribution follows the gaussian function described in Equation 19.

$$\boldsymbol{CO_2(z) = d + a \cdot \exp\left[-\left(\frac{(z-b)^2}{2 \cdot c^2}\right)\right]} \tag{19}$$

where $\boldsymbol{a}$ represents the magnitude of the CO_2 peak, $\boldsymbol{b}$ specifies the altitude of the peak, $\boldsymbol{c}$ controls how spread is the peak (from a slow increase and decrease across multiple layers to an acute peak in few levels), and $\boldsymbol{d}$ shows the CO_2 concentration far enough from the peak. In this study, $\boldsymbol{d}$ always equals to the prior CO_2 knowledge value of 420 ppmv.

The bell-shaped profiles were divided in two categories: the profiles in which the CO_2 peak occurs below the atmospheric boundary layer, which is defined to be at 2 km, called B-ABL, and the profiles where the peak is above the ABL, called A-ABL. The choice of ABL height was based on the upper most height that the ABL usually is (National Oceanic and Atmospheric Administration, n.d.), since the objective of this separation is to see if the retrieval is capable of differentiating the two cases and AERI is most sensitive near the ground, so a higher ABL can be considered a more difficult situation to resolve.

3.6 Radiance Closure

Although the focus of this study is on the synthetic spectral data CO_2 retrieval, the developed algorithm was applied to real AERI data to attest its applicability. For this, a clear-sky field campaign that utilized both a radiosonde balloon launch and CO_2 measurements using a Picarro instrument mounted on the Twin Otter research aircraft from the National Research Council of Canada (NRC) is the main validation method. The site of the campaign is Gault Nature Reserve of McGill University (45.53° N, 73.15° W), which is located right outside of Montreal, Canada. The aircraft started its spiral up trajectory over Gault's site at 08:32 AM Eastern Standard Time (EST) on February 21st, 2024, lasting 15 minutes and covering an altitude range of 0.335 km to 3.078 km. The time of the balloon launch was the same as the start of the spiral.

A radiance closure test was first conducted to assess the agreement between the forward model (LBLRTM) and AERI's spectral measurements, followed by the retrieval. Radiance closure refers to when measurements of a radiometer is compared to a synthetic simulated spectra produced by a radiative transfer model using as close to real atmospheric inputs as possible, in order to verify its accuracy and the consistency between the two (Liu et al, 2024). This is an essential verification step for the retrieval, because if the radiative transfer model is not able to simulate measured spectra with good agreement, then this inconsistency will make the retrieval not possible due to a lack of conversion between estimated and "true" radiance, the $\boldsymbol{F(x_i)}$ and $\boldsymbol{y}$ terms in Equation 5.

The radiosonde used in the balloon launch was an iMet-4 from InterMet. The total error of the instrument was incorporated on the radiative closure tests, they consist of 0.5 K above and 0.95 K below 100 hPa for temperature, and 5% of measured relative humidity, both at 95 % confidence level (InterMet, n.d.). Because the radiosonde drifts, covering areas that are different from that of the launch, a spatial variability uncertainty must also be incorporated on the radiance closure. For this purpose, an ERA5 hourly-mean profile within the 3 × 6 grid boxes rectangular region that includs the balloon trajectory was used to represent the spatial variability of the radiosonde temperature and relative humidity.

Ozone and methane concentrations were obtained from the ERA5 reanalysis dataset and the Copernicus Atmosphere Monitoring Service (CAMS) multi-level global atmospheric composition forecast dataset (Inness et al., 2019), respectively. The instrument used to measure CO_2 was the Picarro G2201i cavity ring-down spectrometer in the CO_2 – CH_4 simultaneous measuring mode, which has an uncertainty of 200 ppb + 0.05% of reading for ^{12}C isotope with 95% confidence (Picarro, n.d.). This CO_2 profile is considered to be the "true" atmospheric state, and (alongside the other atmospheric variables described in this section) is the input for the radiative closure test.

The input profile has a higher vertical resolution in the lower troposphere when compared to upper layers, since this is the region where the ground-based AERI instrument is most sensitive to (Turner & Blumberg, 2018). For CO_2 specifically, a Jacobian calculation using LBLRTM also shows a higher sensitivity at lower levels, which further contributes for the vertical resolution choice.

Regarding AERI's measurements, first the data was treated to avoid erroneous data, such as checking for hatch status and evaluating the sky view noise equivalent radiance. Then, following the method applied by Liu et al. (2024), the 20 s AERI spectra from rapid sampling mode is averaged for a period of 2 minutes before and 8 minutes after the balloon launch, as to provide consistency with the measuring time of the radiosonde and to capture the atmospheric characteristics within the boundary layer.

The AERI spectra collected during the flight time of the field campaign was filtered in order to have only clear-sky cases. The criteria used for the selection was that the brightness temperature difference between the simulated spectra and the AERI measurements at 898 cm^{-1} should be equal or less than 15 K. The 898 cm^{-1} channel was chosen due to it being a very clean channel on the window band (Cox et al., 2015), allowing for it to be used in detecting presence of clouds. The relatively large value of 15 K difference was chosen because, in clear-sky conditions, the window band has low brightness temperature values, meaning that even a small radiance difference can lead to large brightness temperature differences (Liu et al., 2024).

The radiance bias for the radiative closure evaluation for each wavenumber $\boldsymbol{\nu}$ is defined as the measured radiance by the AERI instrument minus the calculated radiance by the radiative transfer model LBLRTM, as represented in Equation 20.

$$\boldsymbol{\Delta R_{\nu} = R_{AERI,\nu} - R_{LBLRTM,\nu}} \tag{20}$$

The bias uncertainty is defined as the root sum square of both the AERI uncertainty, and the uncertainties related to the LBLRTM simulation, as seen in Equation 21:

$$\boldsymbol{\sigma_{\Delta R_{\nu}} = \sqrt{{\sigma_{R_{AERI,\nu}}}^2 + {\sigma_{R_{LBLRTM,\nu}}}^2}} \tag{21}$$

According to Knuteson et al. (2004a), AERI's 3-σ uncertainty (meaning a 99.7% confidence) is calculated as 1% of its ambient blackbody radiance. The model uncertainty is calculated based on the atmospheric inputs uncertainty previously discussed, both from the measuring instruments themselves and the spatial variability from the radiosonde drift for temperature and relative humidity.

In total, 1000 atmospheric profiles were created using randomly generated noise that accounts for all the errors on the model input. By applying radiative Jacobians of CO_2, temperature, and water vapor, the radiance difference between the original and the randomly generated atmospheric profiles was calculated. The standard deviation of these values was used to represent the model 1-σ uncertainty. As to be consistent with AERI's uncertainty, this quantity was converted to 3-σ uncertainty.

3.7 Real Data Retrieval

The AERI radiance spectrum used for the retrieval is the same as the one described in section 3.6, so a spectrum that represents the beginning of the spiral-up flight and also with no clouds in the field-of-view of the instrument.

Different sets of channels for the retrieval were tested. CO_2 has a strong absorption band at 667 cm^{-1}, and two weaker bands centered at 961.0 and 1064 cm^{-1} (Liou, 2002). When evaluating the spectral signature of CO_2 (Figure 2), we see the channels that respond to concentration changes, in particular, the wings of the 667 cm^{-1} absorption band have the highest response.

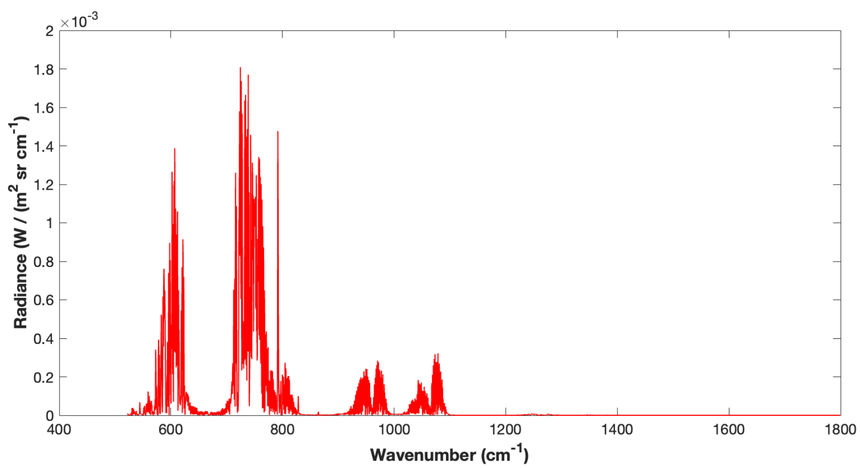

Figure 2. Spectral signature of CO_2 from a 21 ppm perturbation. The main three absorption bands of CO_2 in the mid-infrared region are clearly visible.

Although using all of these wavenumbers would be ideal, the value uncertainty of other variables (such as temperature and water vapor) limits the channel selection. A CO_2 only retrieval means that just CO_2 values are updated at each iteration step, so using wavenumbers that are also sensitive to other atmospheric parameters requires these values to be extremely precise, which sometimes is not possible.

With this in mind, the channel selection avoided bands that are known to be influenced by other gases (e.g., the 9.6 μm absorption band of O_3), and took into account the required precision for channels that are impacted by other atmospheric variables, such as the wavenumbers around the center of the 667 cm^{-1} band that are influenced by surface temperature. The final selection shown in this study comprises the wings of the 667 cm^{-1} band, from 626.3 to 631.6 cm^{-1} and between 707.8 and 721.3 cm^{-1}.

4. Results and Discussion

4.1 Analysis of Different Instrument Settings

Table 2 displays the Cumulative Degrees of Freedom for Signal (CDFS) and the mean RMSE between 0 and 11 km since the troposphere is the region of most interest for the retrieval. The mean RMSE for the prior profile (which is used as first guess in the retrieval) is 17 ppmv.

Table 2. Distinct real and hypothetical instrument simulations results.

Case Number	CDFS	RMSE (ppmv)
1	4.34	2.4587
2	3.91	3.5075
3	2.54	6.5796
4	3.41	4.7763
5	3.05	5.5692
6	2.10	9.3614
7	3.18	5.5826
8	2.81	5.4903

As seen in Table 2, the ideal conditions of Case 1 significantly improve the retrieval, both in terms of information acquired (one degree of information more than the real AERI simulation from Case 5) and in reduction of uncertainty for the CO_2 profile, which is represented by the lower RMSE. By comparing the difference between the RMSE of Cases 3 and 5 with the difference between Cases 2 and 5, it is safe to conclude that the wavenumber resolution has a higher impact on the performance improvement than the noise level. However, instrument noise is still a significant variable for retrieval capacity, as observed by the poorer performance of Case 3 contrasted with the other cases.

We also see the importance of spectral coverage for the retrieval, demonstrated by the significant drop in gained information and uncertainty reduction in Case 6 when compared with the other simulations. This is an important factor to take into consideration when performing the retrieval with real data, because although channels strongly influenced by other atmospheric variables should ideally be avoided, this comes at the cost of retrieval precision and information gained.

Cases 7 and 8 exhibits that summer conditions may favor the retrieval, represented by more information gained (CDFS) of Case 7 when compared to Case 8 and Case 5. The difference in CDFS, however, does not directly translate to a better retrieval performance, as seen by the similar RMSE values in the three cases. This suggests that, although atmospheric conditions influence the retrieval, it does not play a significant role in the accuracy of the retrieved profile when such variables are perfectly represented in the model.

Figure 3 illustrates how the first six cases retrieve a true constant CO_2 profile of 430 ppmv. We can see that Case 1 performs the best, with levels up to 6 km staying within around 1 ppmv from the truth, and Case 6 performs is the most limited, with improvements in the CO_2 profile being limited only in the lower troposphere. The somewhat similar behaviour of Cases 1 to 5 when compared to Case 6 suggests that, if the background atmospheric conditions are perfectly known, using a larger number of channels will have the greatest effect in the retrieval.

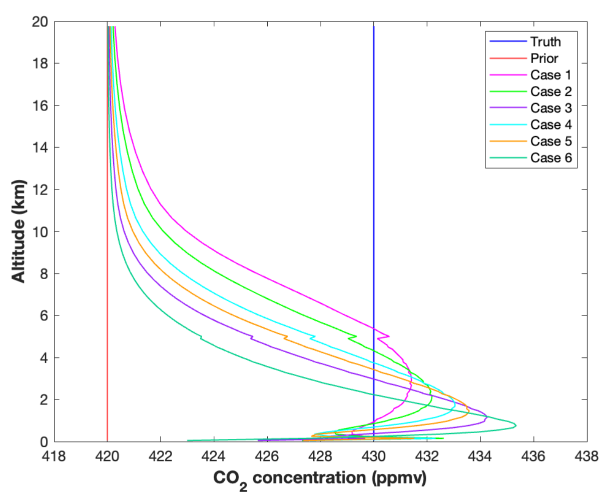

Figure 3. Retrieval of Cases 1 to 6 for a CO_2 constant profile of 430 ppmv.

Since we are mostly interested on the simulation of real AERI specifications, is worth analyzing Case 5 in more detail. The retrieval achieves its first degree of freedom (Figure 4) very close to the surface, at around 100 m height, showing that the first two levels (0 and 0.1 km) can be considered one independent piece of information. The second degree of freedom is reached at around 1 km, and the third one at 7 km. This indicates a potential of the retrieval being able to differentiate distinct CO_2 values below and above the Atmospheric Boundary Layer (ABL), which usually has a height between 1 to 2 km (National Oceanic and Atmospheric Administration, n.d.). The capability of the retrieval in distinguishing CO_2 profiles below and above the ABL is further investigated in section 4.2.

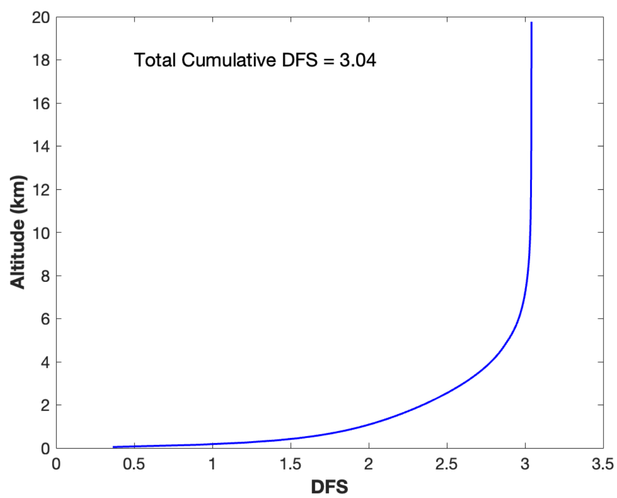

Figure 4. Cumulative Degrees of Freedom for Signal (CDFS) for the real AERI specifications simulation.

The rows of the averaging kernel (Figure 5) show how lower levels have a higher information content that comes from the level itself, with some having more than 40% of the information coming from the appropriate level. This is expected due to AERI being a ground-based instrument and, therefore, is able to see better levels near the surface. However, Figure 5 also demonstrates how the second assigned level (100 m) has a greater averaging kernel value than the surface (0 m). As it will be further discussed in section 4.2, this is likely due to the Jacobian having a lower than presumed sensitivity for the very first retrieval level.

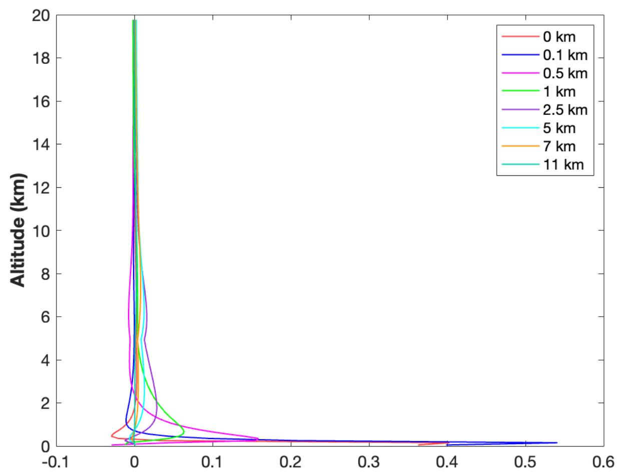

Figure 5. Averaging kernel for the real AERI specifications simulation.

4.2 Analysis of Different CO_2 Profiles

For all the experiments, the prior CO_2 profile is set to be a constant concentration of 420 ppmv for all vertical levels. This choice is based on the knowledge that CO_2 tends, on a yearly average, to have similar concentrations in different heights (Biraud et al., 2013), and that the average CO_2 concentration of Canada in 2022 was around 420 ppmv (Environment and Climate Change Canada, 2023). Moreover, these experiments use the same settings that simulate the real AERI configuration.

The first case evaluated is when the true CO_2 concentration profile is a constant value, like the prior. The concentrations range from 360 ppmv to 480 ppmv, meaning a ± 70 ppmv from the prior, which is greater than the set CO_2 variability of 5% of the total concentration on each layer. This was done to cover most of the possible cases when it comes to this profile shape. The concentrations were randomly generated in a normal distribution around the 420 ppmv value. The true and the retrieved profiles can be seen in Figure 6, and the bias results are shown in Figure 7.

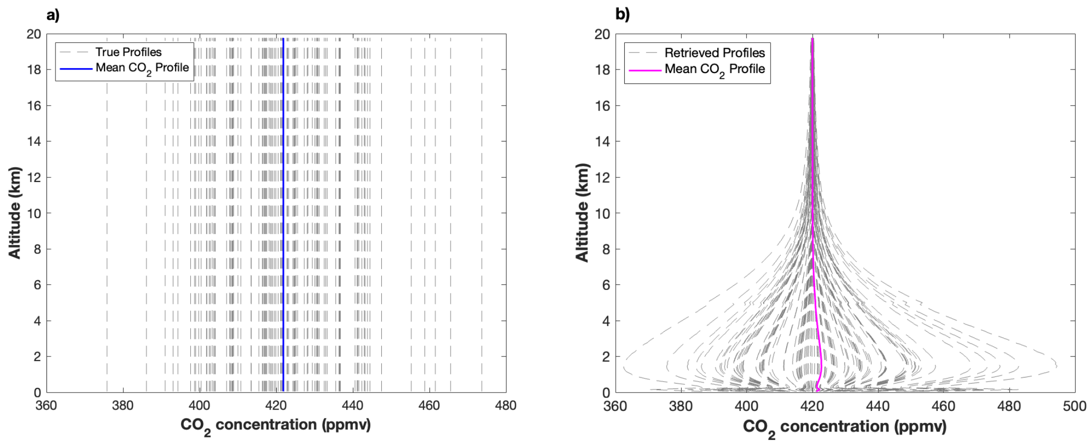

Figure 6. Constant shape case a) true CO_2 profiles, and b) retrieved CO_2 profiles.

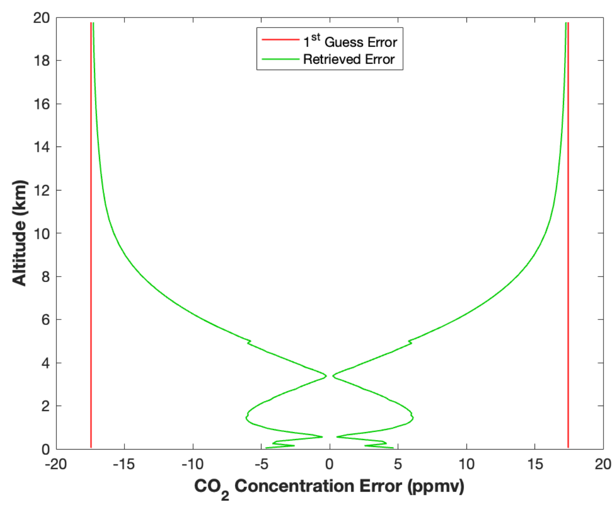

Figure 7. RMSE of mean constant CO_2 profiles.

As seen in Figure 6, the lower portion of the troposphere (from surface to around 5 km) are the levels best sounded by the retrieval. This makes sense because AERI is a ground-based remote sensor and, as such, levels closer to the surface are best seen by the instrument. Moreover, we see a slight singularity at around 5 km where the retrieval does not follow the pattern seen in other levels. This is likely a numerical issue due to the assigned thickness of each layer starting to increase at 5 km.

Figure 7 shows that, for all evaluated levels, the retrieval reduces the uncertainty in the CO_2 profile, with a greater reduction at levels below 4 km. As indicated by the values of the averaging kernel, the vertical resolution is not high enough to resolve quantities on smaller layers, leading to more extreme estimations on certain levels, most notably right below 2 km. This illustrated by the "wiggle" shape of the retrieval error, and an example retrieval for this shape is exhibited in Figure 8.

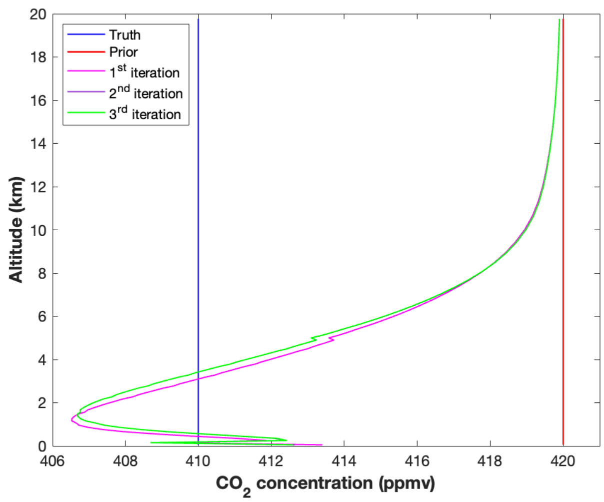

Figure 8. Example of retrieval for constant.

The decreasing (Figure 9) and increasing (Figure 10) profiles display similar patterns to each other, which is expected due to their similar characteristics. The retrieval accurately differentiates the two shape types, and this can be useful when estimating the CO_2 profile in the winter and the summer, as they tend to have a similar pattern to the decreasing and increasing shapes, respectively (Biraud et al., 2013). We see that both cases slightly underestimate the CO_2 value on the very first layer, which could be due to the Jacobian sensitivity being slightly lower at this level compared to the ones right above it (Figure 11). Note that the Jacobian in Figure 11 represents the radiance change in response to the CO_2 perturbation according to the specific vertical layer's resolution used in the retrieval.

For the calculation of the analytical Jacobian using LBLRTM, a level atmospheric input was used. This means that when the radiative transfer model calculates the molecular density and optical depth at each layer, it can underestimate these values on the very first one because of lack of information in two adjacent levels. To minimize this effect, two possible solutions are to increase the vertical resolution at the bottom (so a smaller vertical layer is affected by this issue), or to attempt a layer wise atmospheric description on the LBLRTM.

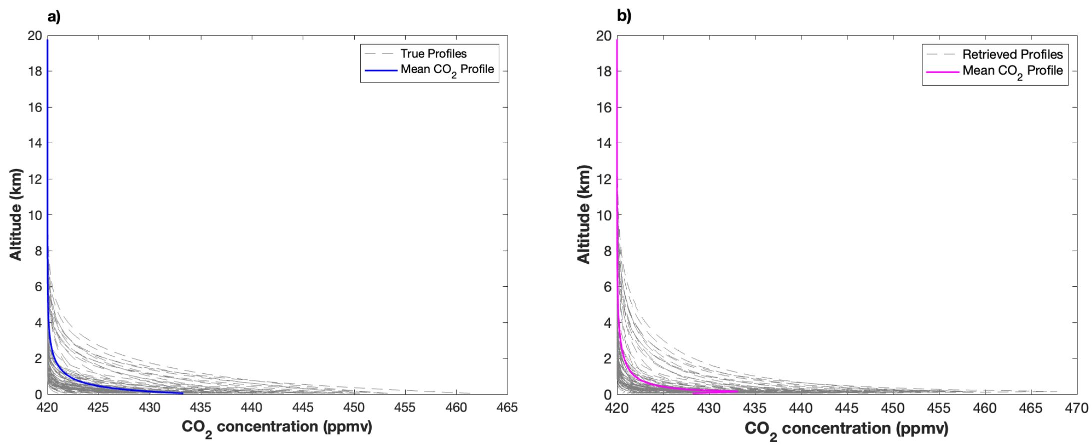

Figure 9. Decreasing shape case a) true CO_2 profiles, and b) retrieved CO_2 profiles.

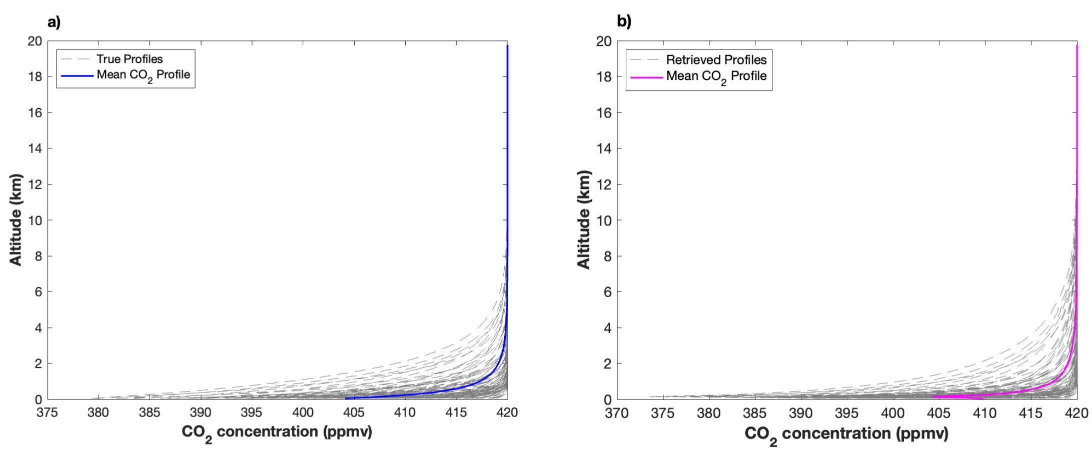

Figure 10. Increasing shape case a) true CO_2 profiles, and b) retrieved CO_2 profiles.

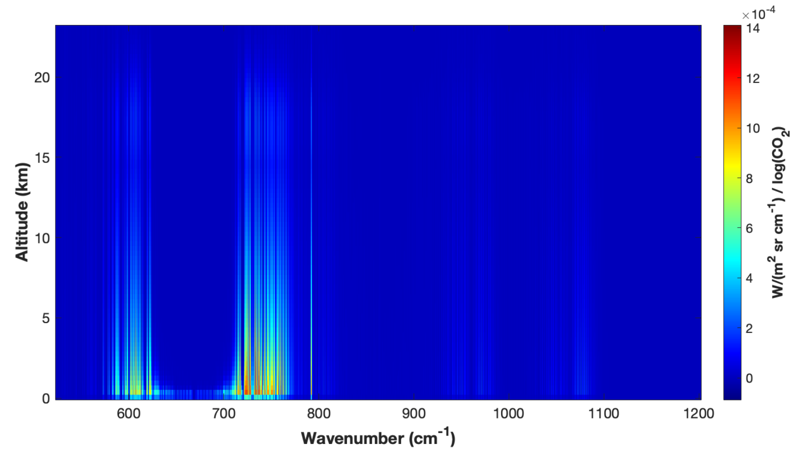

Figure 11. Jacobian of CO_2.

We see that the uncertainty reduction for the decreasing and increasing profiles (Figure 12) is greater than the constant shape, with multiple lower tropospheric levels having close to zero error. This is likely due to the description of the profiles being overall closer to the prior information since, as described by Ghadikolaei (2017), Equation 18 is designed to give realistic changes of atmospheric CO_2, and its values usually does not differ greatly from the mean column concentration at higher altitudes (O'Dell et al., 2012). We also see that the error on the first layer is significantly higher than the ones right above it, which reflects the issue previously discussed about the level calculation on the radiative transfer model.

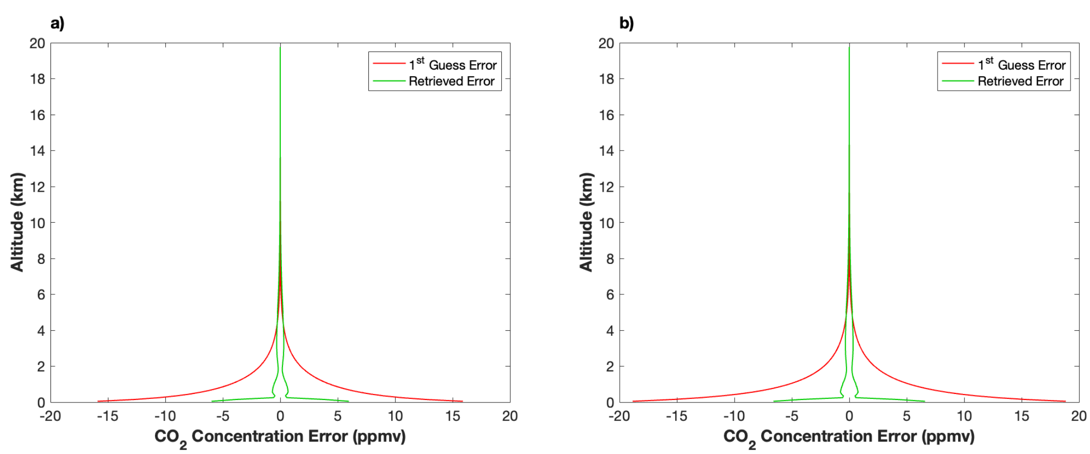

Figure 12. RMSE of mean a) decreasing and b) increasing CO_2 profiles.

The final case is the bell-shaped profiles. From Figure 13, we see that the average peak height for the A-ABL cases was 2.8 km, while for the B-ABL profiles was 1.1 km. We also see that the retrieval can differentiate the two cases by providing distinct profiles, but it tends to underestimate the altitude of the peak (more pronounced for the A-ABL profiles). This can still be useful in determining emission sources, as the knowledge of a CO_2 plume above the ABL combined with wind speed and direction data can indicate the direction where CO_2 emission outside of the measuring location mostly occurs (Xia et al., 2022).

Moreover, we see a pattern of the higher altitude the CO_2 peak occurs, the more the retrieval underestimates the magnitude of the peak, as well as "spreading" the greater CO_2 concentrations across multiple altitudes (the bell-shape is larger). This makes sense considering that the retrieval is most sensitive at the lower layers, and since the retrieval has a lower vertical resolution than the assigned layers, it can interpret a high sharp CO_2 peak as a blunt, lower CO_2 peak.

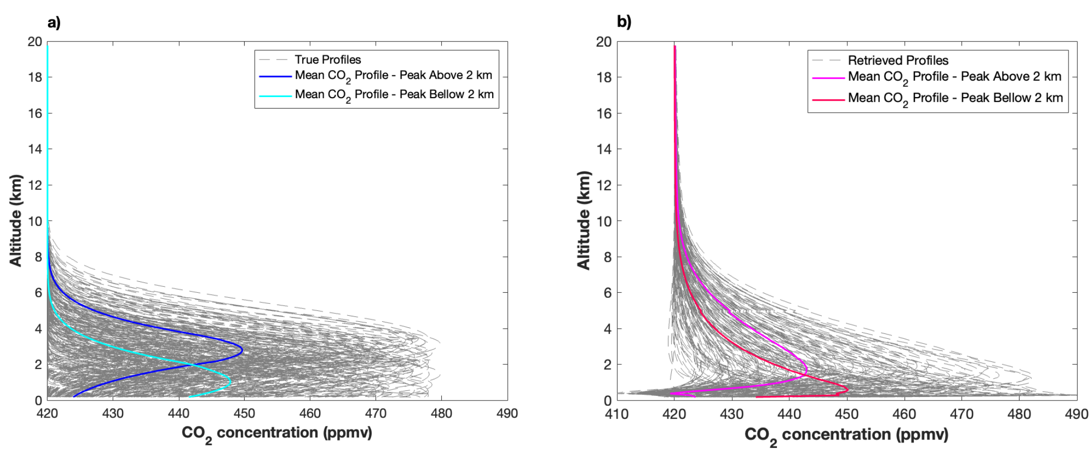

Figure 13. Bell-shaped cases a) true CO_2 profiles, and b) retrieved CO_2 profiles.

The CO_2 profile uncertainty (Figure 14) for both cases is reduced on the lowermost atmospheric layers (up to 4 km for the B-ABL cases and up to 6 km for A-ABL), which shows the usefulness of the retrieval in estimating CO_2 concentrations. However, it also demonstrates that, after a certain point, the retrieval increases the error of the profile. This occurs because, as previously discussed, the retrieval tends to spread the larger CO_2 concentrations over more levels due to its lower vertical resolution than the assigned layers in the retrieval and indicates that the retrieval should be mainly used for estimations in the lower troposphere.

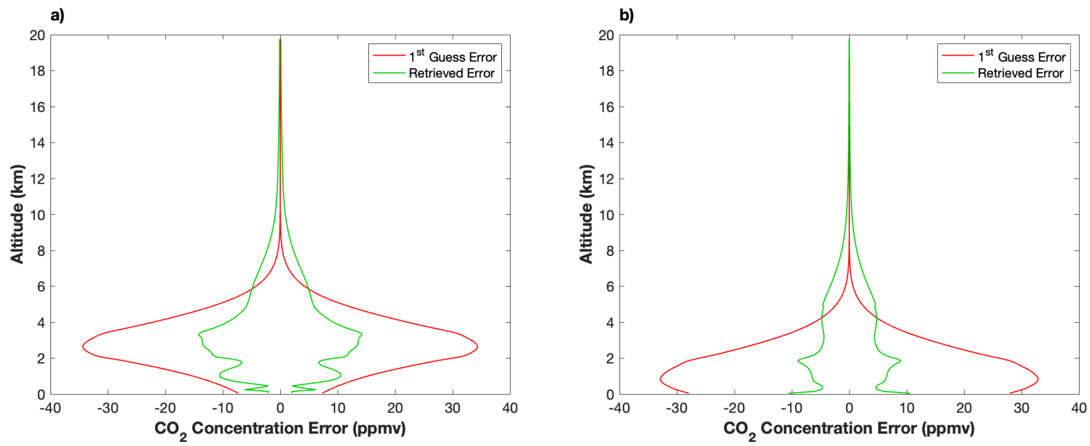

Figure 14. RMSE of mean bell-shaped a) above ABL and b) below ABL CO_2 profiles.

This is not to be confused with the retrieval increasing the uncertainty when compared to the prior information. To evaluate this aspect of the retrieval, a comparison between the prior ($\boldsymbol{S_a}$) and posterior ($\boldsymbol{S}$) uncertainties needs to be made. The retrieval error depicted in Figure 14 having a higher error than the first guess at higher levels is due to the retrieval having a lower vertical resolution than the implemented on the model and does not invalidate the benefits of the retrieval seen in lower levels.

For the bell-shaped case, which is also true for all the other experiments tested, the posterior uncertainty is either equal to or smaller than the prior uncertainty (Figure 15). We see that the greatest reduction occurs near the surface, where the retrieval is most sensitive to, and then decreases until around 5 km, where it becomes the same value as the prior. This corroborates with the discussed implication that the retrieval should be applied for the lower troposphere CO_2 profile.

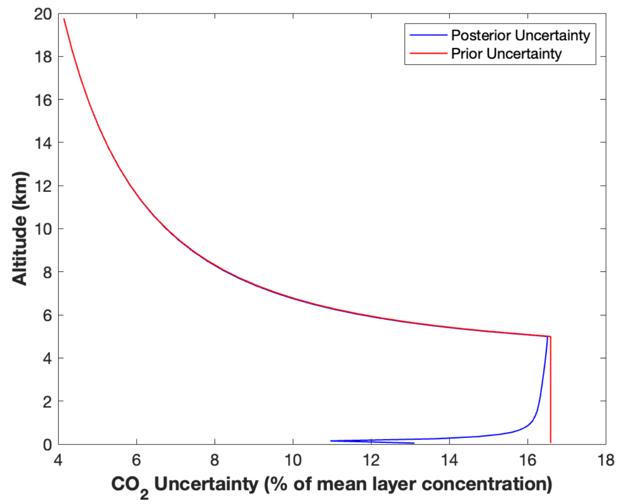

Figure 15. Prior and posterior uncertainties of the retrieval, using Jacobian of bell-shaped case.

4.3 Real Data Radiance Closure

Figure 16 exhibits AERI's radiance closure test results. We see that the model uncertainty is overall about the same or higher than AERI's uncertainty, with the highest values coming from the water vapor channels below 600 cm^{-1}, while the lowest are located on channels above 1400 cm^{-1}.

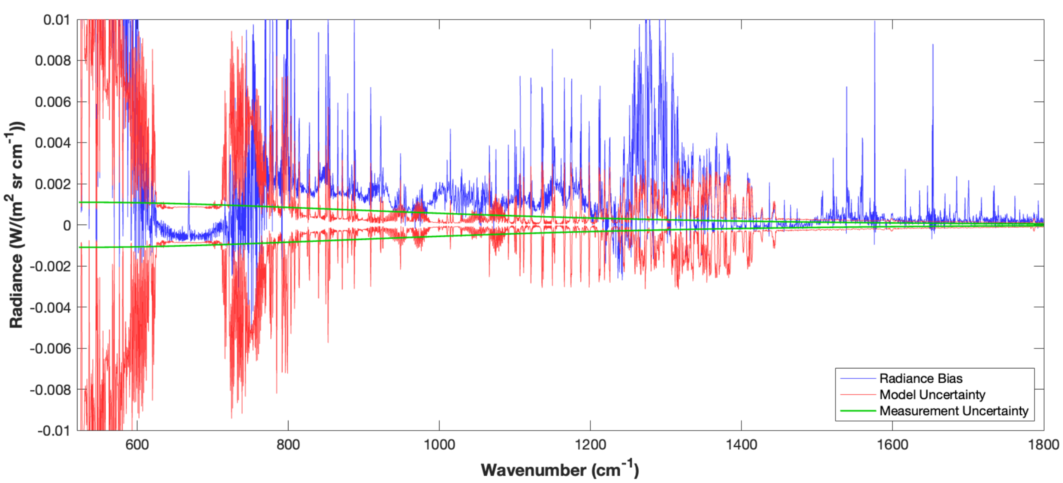

Figure 16. AERI's radiative closure results for the field campaign.

We also observe high uncertainty values on the wings of the CO_2 667 cm^{-1} absorption band which, as expected, is mainly caused by errors in the Picarro measurements of CO_2. The channels of interest for the retrieval due to their sensitivity to CO_2 (between 600 to 800 cm^{-1}) mostly stay within the uncertainty range, especially those on the 620 – 720 cm^{-1} range, indicating that no systematic biases will need to be taken into consideration when making use of these channels.

Channels belonging to the absorption bands of greenhouse gases that were not measured on site exhibits a higher radiance bias than the uncertainty, which makes sense, as the concentration of these gases either were included representing an average over a large area (O_3 and CH_4) or were not included in the LBLRTM simulation (e.g., CFCs and N_2O). We see this primarily for the O_3 1042 cm^{-1} and the 1306 cm^{-1} CH_4 absorption bands.

A systematic positive bias in the window band (800 to 1250 cm^{-1}) is also seen. Other studies have noticed this systemic warm bias in AERI's measurements under clear-sky conditions (Liu et al., 2024; Liu et al., 2022; Delamere et al., 2010). There are a few hypotheses that could explain this positive bias, such as the presence of optically thin clouds and the partial obstruction of AERI's field-of-view (Liu et al., 2024), but no definitive answer to explains this phenomenon has been established. Because the CO_2 retrieval does not utilize channels in the window band, no correction to this warm bias was necessary.

4.4 Real Data Retrieval

The clear-sky conditions of the field campaign were verified through AERI's radiance spectra. Because the forward model (LBLRTM) is set to have no clouds, it is extremely important that AERI's measurements also have this characteristic. Because cloudy and clear-sky radiances have very distinct values in multiple channels, especially in the window band (Figure 17), the conversion of the retrieval is dependent on the cloud conditions of the taken measurement.

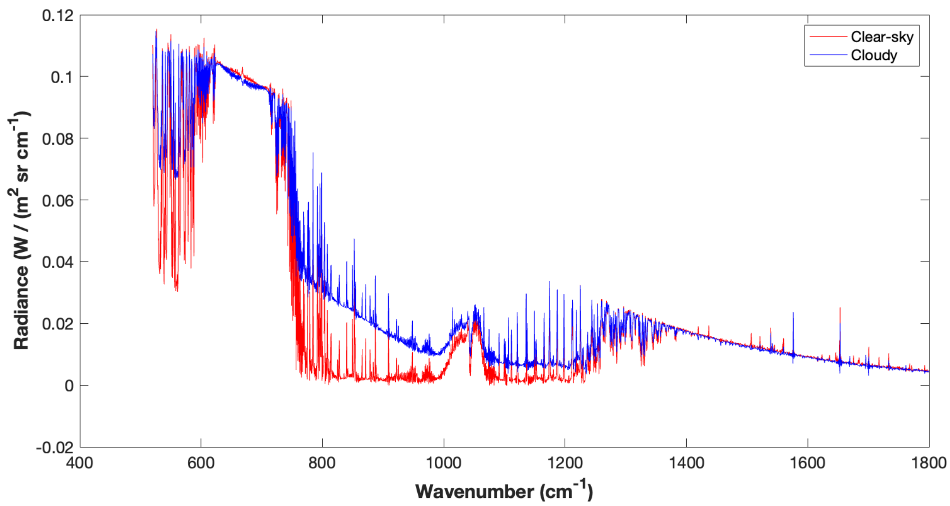

Figure 17. Example of clear-sky and cloudy sky measurements of AERI.

Applying the criteria described in section 3.6, we get 10 minutes averaged spectra shown in Figure 18. As seen by the low radiance values in the window band, the radiance used in the retrieval represents clear-sky conditions.

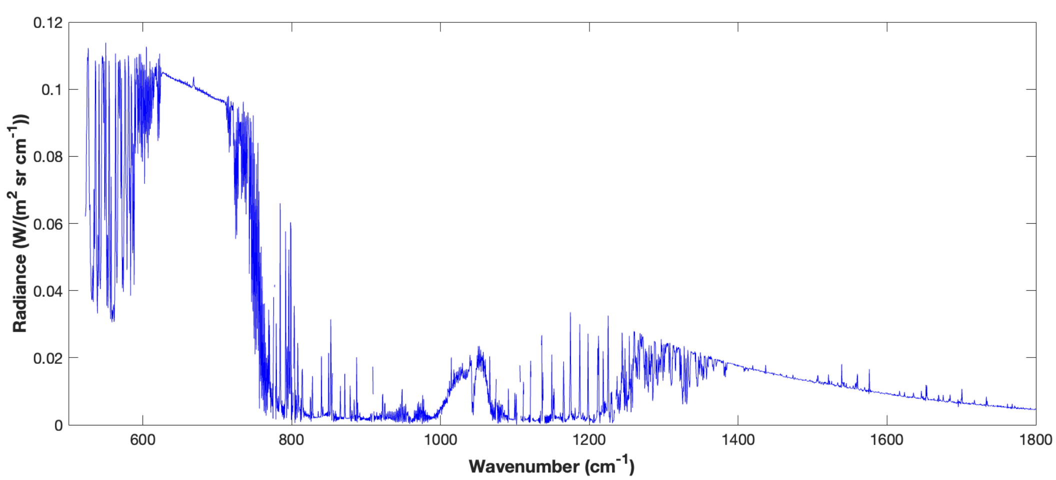

Figure 18. AERI radiance used for CO_2 retrieval. Note that the full spectrum is being showcased, but the retrieval uses a few selected channels.

As with the synthetic experiments, the first guess of the retrieval is the prior knowledge, a constant CO_2 profile of 420 ppmv, and the true CO_2 profile was considered to be a combination of the measurements made by the Picarro on the ground and on the research aircraft (Figure 19). Multiple sets of channels which CO_2 is sensitive to (Figure 2) were tested, and the retrieval that arrived closest to the true profile used the wings of the 667 cm^{-1} CO_2 absorption band (626 – 632 cm^{-1} and 708 – 721 cm^{-1}), with this retrieval being shown in Figure 20.

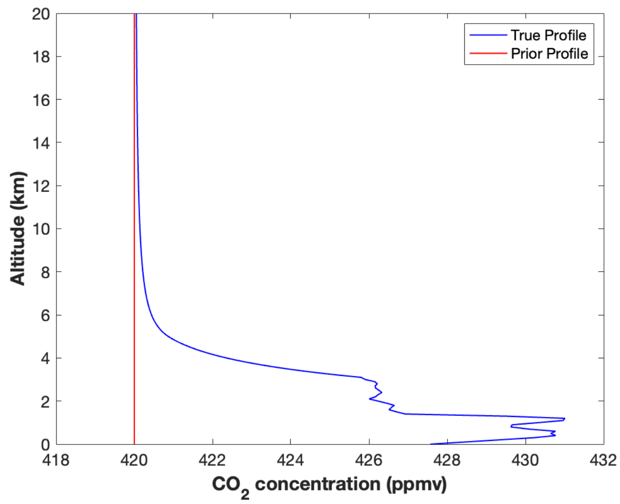

Figure 19. Prior and true CO_2 profiles for retrieval and validation.

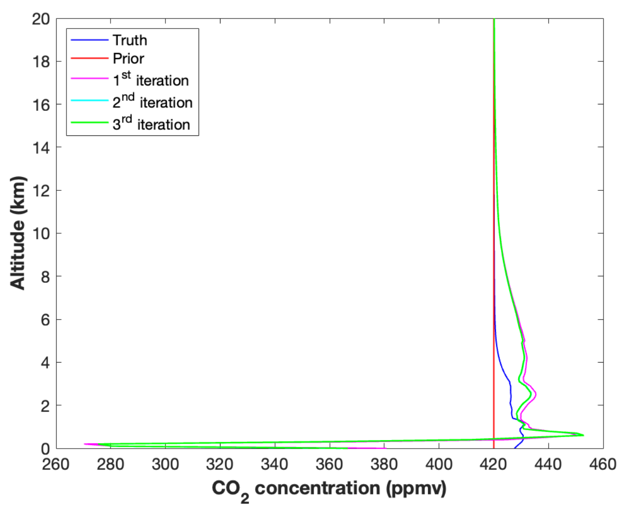

Figure 20. CO_2 retrieval using real AERI measurements.

It is immediately noticeable the unphysical concentration values near the surface up to around 500 m height. This is likely caused by the uncertainty on the temperature profile, which will be discussed in depth later on. If these first layers are not considered (Figure 21), we do see some improvements from the prior profile, in particular between 800 m and 2.5 km. This supports the potential of the retrieval in estimating the CO_2 profile along the lower troposphere, as long as the issues with surface unphysical values is solved. It is also worth remembering that CO_2 measurements for validation are limited to the first 3 km of the atmosphere, so there is a possibility that the retrieval captures CO_2 values above this level better than is shown in Figure 21.

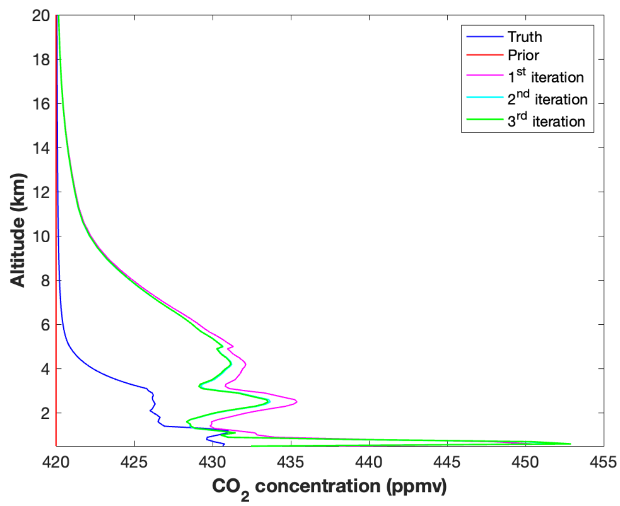

Figure 21. CO_2 retrieval using real AERI measurements from 0.5 to 10 km.

The channels around the main CO_2 absorption band are also strongly influenced by temperature, as seen in Figure 22, which shows the sensitivity of each wavenumber to temperature. Because the retrieval only adjusts values of CO_2, even small errors in the temperature profile can lead to great discrepancies in CO_2 value, as the model tries to adjust the radiance value difference that is being caused by temperature with extreme CO_2 concentrations.

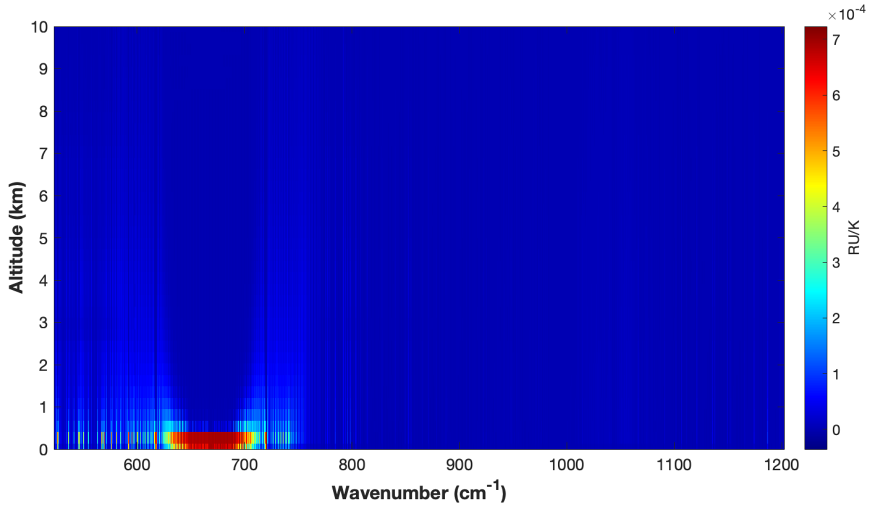

Figure 22. Jacobian of temperature for first 10 km, which represents the channels sensitivity to temperature.

Uncertainties in temperature comes not only in a measuring instrument itself (e.g., the 0.5 K uncertainty for the radiosonde measurements above 100 hPa), but also between instruments and measuring techniques, as illustrated in Figure 23. The temperatures used for Figure 23 are described in Table 3, and all of them were collected at the closest available time of the balloon launch on the field campaign for each dataset.

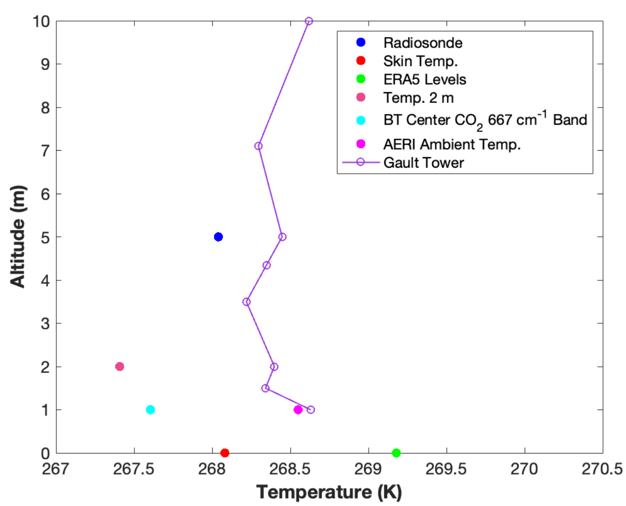

Figure 23. Surface temperature measurements of different instruments and reanalysis techniques for the time of the field campaign.

Table 3. Description of temperature values used in Figure 23.

Variable Name	Data Origin	Description
Radiosonde	iMet-4	Radiosonde reading on field campaign
Skin Temp.	ERA5	Skin temperature from ERA5 single levels
ERA5 Levels	ERA5	Surface temperature obtained from extrapolation of ERA5 pressure levels temperature profile
Temp. 2 m	ERA5	2 m temperature from ERA5 single levels
BT Center 667 cm^{-1} Band	AERI	Brightness temperature of AERI'S 667 cm^{-1} channel
AERI Ambient Temp.	AERI	AERI ambient thermometer reading
Gault Tower	EOS	Temperature from meteorological tower of the Earth Observation System (EOS) at Gault

A synthetic spectra experiment was designed to test this hypothesis. In this experiment, the background atmospheric values of the retrieval first guess and the truth are the same, with the exception of the surface temperature, where its value in the true profile was 0.1 K more than in the first guess. The results of this test are shown in Figure 24.

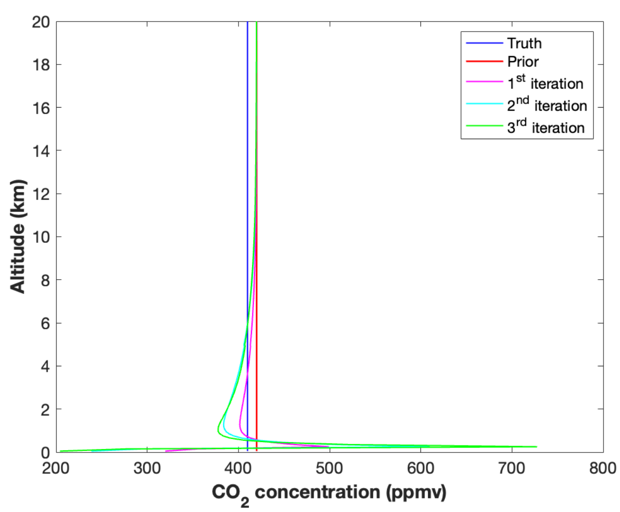

Figure 24. Synthetic spectra retrieval with 0.1 K difference at surface.

The behavior of the retrieval at Figure 24 is very similar to the real data retrieval shown in Figure 20, with near-surface extreme CO_2 values being used to compensate for the radiance difference caused by temperature. As such, an initial joint retrieval of temperature and CO_2 was performed to assess if it improves estimations at lower levels.

The covariance matrix for the a priori knowledge of temperature ($\mathbf{S_a}$ of temperature), which is necessary for the retrieval, was obtained from the 10 years climatology of ERA5 for the month of February in the grid boxes containing Gault's site. In order to prevent the inversion of this matrix to be close to singular, the off-diagonal elements were set to be 99% of their original value.

Because temperature is mostly sensitive to lower atmospheric levels (Figure 22), two sets of experiments were tested. In the first one, the retrieved temperatures for only the lowermost level is used, while the rest of the profile remains the same as used for CO_2 only retrieval. This is to check if a correction at just the surface is sufficient to improve the CO_2 estimation. For the second experiment, the retrieved temperatures for the first five levels (surface to 0.4 km) were applied, while the remaining levels kept their original values. This is to account for the layers that show most sensitivity to temperature, represented by the red color in Figure 22.

Figure 25 depicts the CO_2 retrieval when using the retrieved temperature only for the surface. When comparing to Figure 20, we see some improvement in the retrieved CO_2 profile. Although the extreme values in the lowermost layers persist, the retrieval overall got closer to the truth, as illustrated in Figure 26, with the main exceptions being the very first level and around 1 km, where the true CO_2 profile show a small peak of 430 ppmv that is underestimated by the new retrieval.

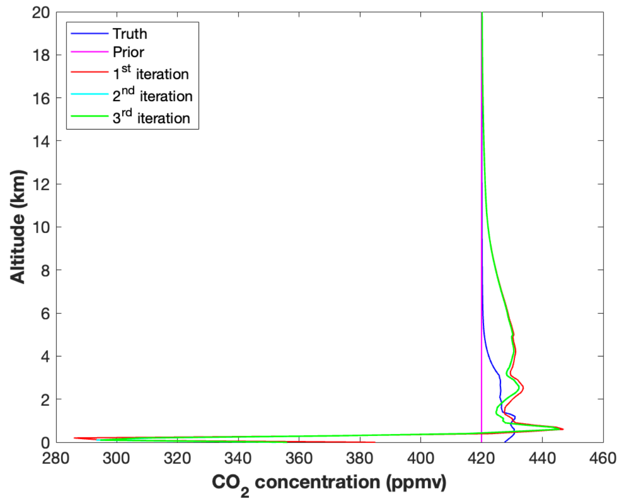

Figure 25. CO_2 retrieval using retrieved temperature for surface level.

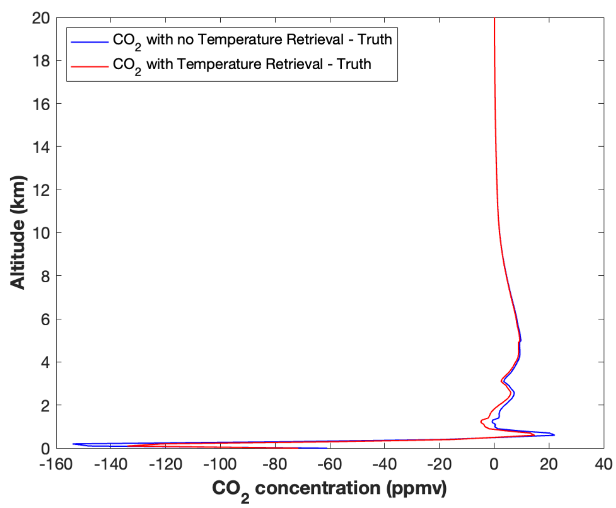

Figure 26. Difference between retrieved and true CO_2 profiles.

Figure 27 presents the CO_2 retrieval when using the retrieved temperature between 0 and 0.4 km. We can see that the retrieval performs worse than the two real data cases presented before, as it greatly underestimates the CO_2 concentration in multiple levels. These results, alongside the one depicted in Figure 25, indicates that either the joint retrieval technique needs to be refined for a more accurate profile, or that other factors might also be influencing the results.

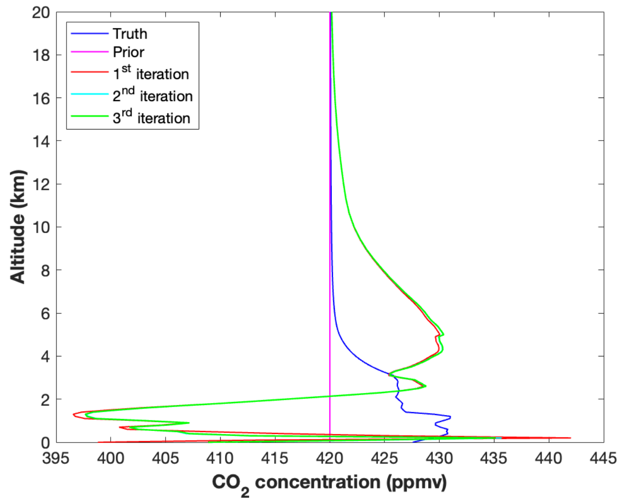

Figure 27. CO_2 retrieval using retrieved temperature between 0 and 0.4 km.

Other works have found similar issues with retrieving CO_2 from ground-based remote sensing instruments when temperature is considered an unknown variable (Ghadikolaei, 2017; Roche et al., 2021). Suggestions to improve the retrieval capabilities include using a fixed CO_2 surface value collected from an in-situ instrument, which would give the algorithm a starting point to adjust the CO_2 profile with the measured radiance, and to utilize principal component analysis for noise reduction in AERI's measurements (Turner et al., 2006; Ghadikolaei, 2017).

One aspect that could also be explored in future research is how to assign the $\mathbf{S_a}$ matrix for the CO_2 retrieval. Maahn et al. (2020) analyzed how the lack of off-diagonal elements in the $\mathbf{S_a}$ matrix for humidity led to the retrieval staying closer to the prior H_2O values and a lesser reduction of the uncertainty when compared to using a $\mathbf{S_a}$ with off-diagonal values, which could be the case for CO_2 as well. Moreover, CO_2 variability at the lower atmospheric levels can be much higher than the 5% that was prescribed, as seen in the work of O'Dell et al. (2012), which can also contribute for a greater weight being put in the prior input when compared to the information from the measurements. As such, different (and more realistic) $\mathbf{S_a}$ settings should be tested.

5. Conclusion

The negative impacts that global warming already had around the globe, alongside the potential of it causing even worst societal issues calls for efforts in better understanding the behaviour of its main culprit, CO_2 emissions (Arias et al., 2021). Although considerable progress has been made in this area, especially regarding measurements from remote sensing instruments, there is still a lack of estimations of CO_2 whole-day vertical profiles for the lower troposphere, which is a knowledge that would help not only in improving CO_2 daily and seasonal cycles implementation in climate models, but also aid in tracking CO_2 emissions and progress of net-zero efforts.

This project aimed to assess the capability of AERI, a Fourier transform spectrometer that measures DLR, in retrieval the vertical profile of CO_2. Synthetic idealized experiments showed that the AERI instrument, with its current specifications, is capable of retrieving CO_2 with an average accuracy of 5.5 ppmv, which is smaller than the natural CO_2 variability in the lower troposphere and supports the conclusion that the retrieval improves the profile estimation when compared to CO_2 prior knowledge.

The synthetic experiments also demonstrated that the retrieval is capable of differentiating distinct profile shapes, including when CO_2 peaks occur above or below the ABL. This means that AERI has great potential to improve the understanding of CO_2 daily cycle by identifying patterns in its concentration distribution depending on the time of the day. This knowledge can also help in determining emission sources since the information of the profiles combined with wind speed and direction data can present clues of the direction where emission mostly occurs (Xia et al., 2022).

When applied to real atmospheric conditions, the algorithm showed potential in retrieving the CO_2 profile when validated against in-situ measurements, especially in the range of 800 m and

2.5 km. Issues with the retrieval at very near surface levels are thought to be caused by not enough accurate temperature readings, which could possibly be solved through the use of a joint temperature and CO_2 retrieval and should be further explored in future work, since the results presented here represent an initial assessment of this influence. Other aspects of the retrieval, such as the prior covariance matrix, should also be analyzed in order to fully understand the potential of using AERI for CO_2 estimations in a North American setting.

Overall, the synthetic experiments present a promising application of AERI in CO_2 vertical profile retrieval, and future work should explore possible influencing factors, such as other atmospheric variables and the setting of the retrieval itself, to overcome current issues in the real data retrieval in order to increase its accuracy.

Bibliography

Allen, M.R., Dube, O.P., Solecki, W., Aragón-Durand, F., Cramer, W., Humphreys, S., Kainuma, M., Kala, J., Mahowald, N., Mulugetta, Y., Perez, R., Wairiu, M., & Zickfeld, K. (2018). Framing and Context. In V. Masson-Delmotte, P. Zhai, H.-O. Pörtner, D. Roberts, J. Skea, P.R. Shukla, A. Pirani, W. Moufouma-Okia, C. Péan, R. Pidcock, S. Connors, J.B.R. Matthews, Y. Chen, X. Zhou, M.I. Gomis, E. Lonnoy, T. Maycock, M. Tignor & T. Waterfield (Eds.), *Global Warming of 1.5°C. An IPCC Special Report on the impacts of global warming of 1.5°C above pre-industrial levels and related global greenhouse gas emission pathways, in the context of strengthening the global response to the threat of climate change, sustainable development, and efforts to eradicate poverty*. Cambridge University Press, pp. 49-92. https://doi.org/10.1017/9781009157940.003

Arias, P. A., Bellouin, N., Coppola, E., Jones, R. G., Krinner, G., Marotzke, J., Naik, V., Palmer, M.D., Plattner, G.-K., Rogelj, J., Rojas, M., Sillmann, J., Storelvmo, T., Thorne, P.W., Trewin, B., Achuta Rao, K., Adhikary, B., Allan, R.P., Armour, K. ... Zickfeld, K. (2021). Technical summary. In V. Masson-Delmotte, P. Zhai, A. Pirani, S. L. Connors, C. Péan, S. Berger, N. Caud, Y. Chen, L. Goldfarb, M.I. Gomis, M. Huang, K. Leitzell, E. Lonnoy, J.B.R. Matthews, T.K. Maycock, T. Waterfield, O. Yelekçi, R. Yu & B. Zhou (Eds.), *Climate change 2021: The physical science basis. Contribution of working group I to the sixth assessment report of the Intergovernmental Panel on Climate Change* (pp. 33–144). Cambridge University Press. https://doi.org/10.1017/9781009157896.002

Arora, V. K., Katavouta, A., Williams, R. G., Jones, C. D., Brovkin, V., Friedlingstein, P., Schwinger, J., Bopp, L., Boucher, O., Cadule, P. et al., Chamberlain, M. A., Christian, J. R., Delire, C., Fisher, R. A., Hajima, T., Ilyina, T., Joetzjer, E., Kawamiya, M., Koven, C. D., ... Zihen, T. (2020). Carbon-concentration and carbon-climate feedbacks in CMIP6 models, and their comparison to CMIP5 models. *Biogeosciences, 17*, 4173–4222. https://doi.org/10.5194/bg-17-4173-2020

Babenhauserheide, A., Hase, F., & Morino, I. (2020). Net CO_2 fossil fuel emissions of Tokyo estimated directly from measurements of the Tsukuba TCCON site and radiosondes. *Atmospheric Measurement Techniques, 13*, 2697–2710. https://doi.org/10.5194/amt-13-2697-2020

Bezyk, Y., Górka, M., Sówka, I., Nęcki, J., & Strąpoć, D. (2023). Temporal dynamics and controlling factors of CO_2 and CH_4 variability in the urban atmosphere of Wroclaw, Poland. *Science of the Total Environment, 893*, 164771. https://doi.org/10.1016/j.scitotenv.2023.164771

Biraud, S. C., Torn, M. S., Smith, J. R., Sweeney, C., Riley, W. J., & Tans, P. P. (2013). A multi-year record of airborne CO_2 observations in the US Southern Great Plains. *Atmospheric Measurement Techniques, 6*, 751–763. https://doi.org/10.5194/amt-6-751-2013

Canadell, J. G., Monteiro, P. M. S., Costa, M. H., Cotrim da Cunha, L., Cox, P.M., Eliseev, A.V., Henson, S., Ishii, M., Jaccard, S., Koven, C., Lohila, A., Patra, P. K., Piao, S., Rogelj, J., Syampungani, S., Zaehle, S., & Zickfeld, K. (2021). Global Carbon and other Biogeochemical Cycles and Feedbacks. In V. Masson-Delmotte, P. Zhai, A. Pirani, S.L. Connors, C. Péan, S. Berger, N. Caud, Y. Chen, L. Goldfarb, M.I. Gomis, M. Huang, K. Leitzell, E. Lonnoy, J.B.R. Matthews, T.K. Maycock, T. Waterfield, O. Yelekçi, R. Yu & B. Zhou (Eds.), *Climate Change 2021: The Physical Science Basis. Contribution of Working Group I to the Sixth Assessment Report of the Intergovernmental Panel on Climate Change* (pp. 673–816). Cambridge University Press. https://doi.org/10.1017/9781009157896.007

Chen, L., Msigwa, G., Yang, M., Osman, A. I., Fawzy, S., Rooney, D. W., & Yap, P.-S. (2022). Strategies to achieve a carbon neutral society: A Review. *Environmental Chemistry Letters*, *20*(4), 2277–2310. https://doi.org/10.1007/s10311-022-01435-8

Chen, Y., Lu, Y., Qi., B., Ma, Q., Zang, K., Lin, Y., Liu, S., Pan, F., Li, S., Guo, P., Chen, L., Lan, W., & Fang, S. (2024). Atmospheric CO_2 in the megacity Hangzhou, China: Urban-suburban differences, sources and impact factors. *Science of the Total Environment, 926*, 171635. https://doi.org/10.1016/j.scitotenv.2024.171635

Cheng, X. L., Liu, X. M., Liu, Y. J., & Hu, F. (2018): Characteristics of CO_2 concentration and flux in the Beijing urban area. *Journal of Geophysical Research: Atmospheres, 123*, 1785–1801. https://doi.org/10.1002/2017JD027409

Crippa, M., Guizzardi, D., Pisoni, E., Solazzo, E., Guion, A., Muntean, M., Florczyk, A., Schiavina, M., Melchiorri, M., & Hutfilter, A. F. (2021). Global anthropogenic emissions in urban areas: patterns, trends, and challenges. *Environmental Research Letters, 16*(7), 074033. https://doi.org/10.1088/1748-9326/ac00e2

Crevoisier, C., Chedin, A., & Scott, N. A. (2003). AIRS channel selection for CO_2 and other trace-gas retrievals. *Quarterly Journal of the Royal Meteorological Society, 129*, 2719–2740. https://doi.org/10.1256/qj.02.180

Crevoisier, C., Heilliette, S., Chédin, A., Serrar, S., Armante, R., & Scott, N. A. (2004). Midtropospheric CO_2 concentration retrieval from AIRS observations in the tropics. *Geophysical Research Letters, 31*(17), L17106.

Crisp, D., Atlas, R. M., Breon, F. -M., Brown, L. R., Burrows, J. P., Ciais, P., Connor, B. J., Doney, S. C., Fung, I. Y., Jacob, D. J., Miller, C. E., O'Brien, D., Pawson, S., Randerson, J. T., Rayner, P., Salawitch, R. J., Sander, S. P., Sen, B., Stephens, G. L., … Schroll, S. (2004). The Orbiting Carbon Observatory (OCO) Mission. *Advances in Space Research, 34*(4), 700–709. https://doi.org/10.1016/j.asr.2003.08.062

Crisp, D., Pollock, H. R., Rosenberg, R., Chapsky, L., Lee, R. A., Oyafuso, F. A., Frankenberg, C., O'Dell, C. W., Bruegge, C. J., Doran, G. B., Eldering, A., Fisher, B. M., Fu, D., Gunson, M. R., Mandrake, L., Osterman, G. B., Schwandner, F. M., Sun, K., Taylor, T. E., … Wunch, D. (2017). The on-orbit performance of the Orbiting Carbon Observatory-2 (OCO-2) instrument and its radiometrically calibrated products. *Atmospheric Measurement Techniques, 10*(1), 59–81. https://doi.org/10.5194/amt-10-59-2017

Clough, S. A., Iacono, M. J., & Moncet, J-L. (1992). Line-by-line calculation of atmospheric fluxes and cooling rates: application to water vapor. *Journal of Geophysical Research, 97*, 15761–15785. https://doi.org/10.1029/92JD01419

Clough, S. A., Iacono, M. J., & Moncet, J. L. (2014). LBLRTM: Line-By-Line Radiative Transfer Model. *Astrophysics Source Code Library*, record ascl:1405.001 (ascl:1405.001)

Colman, R., & Soden, B. J. (2021). Water vapor and lapse rate feedbacks in the climate system. *Reviews of Modern Physics, 93*, 045002. https://doi.org/10.1103/RevModPhys.93.045002

Cox, C. J., Walden, V. P., Rowe, P. M., & Shupe, M. D. (2015). Humidity trends imply increased sensitivity to clouds in a warming Arctic. *Nature Communications, 6*(10117). https://doi.org/10.1038/ncomms10117

Dasgputa, S., Lall, S., & Wheeler, D. (2023). Subways and CO_2 emissions: A global analysis with satellite data. *Science of The Total Environment, 883*, 163691. https://doi.org/10.1016/j.scitotenv.2023.163691

Delamere, J., Clough, S., Payne, V., Mlawer, E., Turner, D., & Gamache, R. (2010). A far-infrared radiative closure study in the Arctic: Application to water vapor. *Journal of Geophysical Research: Atmospheres, 115*, D17106. https://doi.org/10.1029/2009JD012968

Demirgian, J., & Dedecker, R. (2005, January). *Atmospheric Emitted Radiance Interferometer (AERI) Handbook.* https://www.arm.gov/publications/tech_reports/handbooks/aeri_handbook.pdf

Dou, X., Hong, J., Ciais, P., Chevallier, F., Yan, F., Yu, Y., Hu, Y., Huo, D., Sun, Y., Wang, Y., Davis, S. J., Crippa, M., Janssens-Maenhout, G., Guizzardi, D., Solazzo, E., Lin, X., Song, X., Zhu, B. Cui, D. … Liu, Z. (2023). Near-real-time global gridded daily CO_2 emissions 2021. *Scientific Data, 10*(69). https://doi.org/10.1038/s41597-023-01963-0

Engelen, R. J., Andersson, E., Chevallier, F., Hollingsworth, A., Matricardi, M., McNally, A. P., Thépaut, J. -N., & Watts, P. D. (2004). Estimating atmospheric CO_2 from advanced infrared satellite radiances within an operational 4D-Var data assimilation system: Methodology and first results. *Journal of Geophysical Research, 109*, D19309. https://doi.org/10.1029/2004JD004777

Environment and Climate Change Canada. (2023, June 29). *Greenhouse gas concentrations*. https://www.canada.ca/en/environment-climate-change/services/environmental-indicators/greenhouse-gas-concentrations.html

Feltz, W F., Smith, W. L., Knuteson, R. O., Revercomb, H. E., Woolf, H. M., & Howell, H. B. (1998). Meteorological Applications of Temperature and Water Vapor Retrievals from the Ground-Based Atmospheric Emitted Radiance Interferometer (AERI). *Journal of Applied Meteorology and Climatology, 37*, 857–875. https://doi.org/10.1175/1520-0450(1998)037<0857:MAOTAW>2.0.CO;2

Ghadikolaei, K. K. (2017). *CO_2 Profiling in the Lower Troposphere using a High Spectral Resolution Infrared Radiometer*. [Doctoral dissertation, University of Cologne]. Cologne University Publications Server.

Hersbach, H., Bell, B., Berrisford, P., Hirahara, S., Horányi, A., Muñoz-Sabater, J., Nicolas, J., Peubey, C., Radu, R., & Schepers, D. (2020). The ERA5 global reanalysis. *Quarterly Journal of the Royal Meteorological Society, 146*, 1999–2049. https://doi.org/10.1002/qj.3803

Hu, C., Griffis, T. J., Lee, X., Millet, D. B., Chen, Z., Baker, J. M., & Xiao, K. (2018). Top-Down Constraints on Anthropogenic CO_2 Emissions Within an Agricultural-Urban Landscape. *Journal of Geophysical Research: Atmospheres, 123*, 4674–4694. https://doi.org/10.1029/2017JD027881

Hu, K., Zhang, Q., Gong, S., Zhang, F., Weng, L., Jiang, S., & Xia, M. (2024). A Review of Anthropogenic Ground-Level Carbon Emissions Based on Satellite Data. *IEEE Journal of Selected Topics in Applied Earth Observations and Remote Sensing, 17*, 8339–8357. https://doi.org/10.1109/JSTARS.2024.3355549

Huang, W., Liu, L., Yang, B., Hu, S., Yang, W., Li, Z., Li, W., & Yang, X. (2023). Retrieval of temperature and humidity profiles from ground-based high-resolution infrared observations using an adaptive fast iterative algorithm, *Atmospheric Measurement Techniques, 16*, 4101–4114. https://doi.org/10.5194/amt-16-4101-2023

Houghton, J. (2001). The science of global warming. *Interdisciplinary Science Reviews, 26*(4), 247–257.

Imasu, R., Matsunaga, T., Nakajima, M., Yoshida, Y., Shiomi, K., Morino, I. Saitoh, N., Niwa, Y., Someya, Y., Oishi, Y., Hashimoto, M., Noda, H., Hikosaka, K., Uchino, O., Maksyutov, S., Takagi, H., Ishida, H., Nakajima, T. H., Nakajima, T., & Shi, C. (2023). Greenhouse gases Observing SATellite 2 (GOSAT-2): mission overview. *Progress in Earth and Planetary Science, 10*(33). https://doi.org/10.1186/s40645-023-00562-2

Inness, A., Ades, M., Agustí-Panareda, A., Barré, J., Benedictow, A., Blechschmidt, A.-M., Dominguez, J. J., Engelen, R., Eskes, H., Flemming, J., Huijnen, V., Jones, L., Kipling, Z., Massart, S., Parrington, M., Peuch, V.-H., Razinger, M., Remy, S., Schulz, M., & Suttie, M. (2019). The CAMS reanalysis of atmospheric composition. *Atmospheric Chemistry and Physics, 19*, 3515–3556. https://doi.org/10.5194/acp-19-3515-2019

Prentice, I.C., Farquhar, G.D., Fasham, M.J.R., Goulden, M.L., Heimann, M., Jaramillo, V. J., Kheshgi, H.S., Le Quéré, C., Scholes, R.J., & Wallace, D.W.R. (2001). The Carbon Cycle and Atmospheric Carbon Dioxide. In J. T. Houghton, Y. Ding, D.J. Griggs, M. Noguer, P.J. van der Linden, X. Dai, K. Maskell & C.A. Johnson (Eds.), *Climate Change 2001: The Scientific Basis. Contribution of Working Group I to the Third Assessment Report of the Intergovernmental Panel on Climate Change* (pp. 183–238). Cambridge University Press.

InterMet Systems. (n.d.). *iMet-4 Radiosonde*. https://www.intermetsystems.com/products/imet-4-radiosonde/

Japan Aerospace Exploration Agency. (2011, March). *GOSAT / IBUKI Data Users Handbook*. https://www.eorc.jaxa.jp/GOSAT/assets/doc/GOSAT_HB_E_1stEdition_for_HP.pdf

Karbasi, S., Malakooti, H., Rahnama, M., & Azadi, M. (2022). Study of mid-latitude retrieval XCO_2 greenhouse gas: Validation of satellite-based shortwave infrared spectroscopy with ground-based TCCON observations. *Science of the Total Environment, 836*, 155513. http://doi.org/10.1016/j.scitotenv.2022.155513

Keeling, C. D., Bacastow, R. B., Bainbridge, A. E., Ekdahl Jr, C. A., Guenther, P. R., Waterman, L. S., & Chin, J. F. (1976). Atmospheric carbon dioxide variations at Mauna Loa observatory, Hawaii. *Tellus, 28*(6), 538–551.

Knuteson, R. O., Revercomb, H. E., Best, F. A., Ciganovich, N. C., Dedecker, R. G., Dirkx, T. P., Ellington, S. C., Feltz, W. F., Garcia, R. K., Howell, H. B., Smith, W. L., Short, J. F., & Tobin, D. C. (2004a). Atmospheric Emitted Radiance Interferometer. Part I: Instrument Design. *American Meteorological Society, 21*, 1763–1776.

Knuteson, R. O., Revercomb, H. E., Best, F. A., Ciganovich, N. C., Dedecker, R. G., Dirkx, T. P., Ellington, S. C., Feltz, W. F., Garcia, R. K., Howell, H. B., Smith, W. L., Short, J. F., & Tobin, D. C. (2004b). Atmospheric Emitted Radiance Interferometer. Part II: Instrument Performance. *American Meteorological Society, 21*, 1777–1789.

Kuze, A., Suto, H., Nakajima, M., & Hamazaki, T. (2009). Thermal and near infrared sensor for carbon observation fourier-transform spectrometer on the greenhouse gases observing satellite for greenhouse gases monitoring. *Applied Optics, 48*, 6716–6733.

Lewis, W. E., Wagner, T. J., Otkin, J. A., Jones, T. A. (2020). Impact of AERI Temperature and Moisture Retrievals on the Simulation of a Central Plains Severe Convective Weather Event. *Atmosphere, 11*(7), 729. https://doi.org/10.3390/atmos11070729

Li, Y., Deng, J., Mua, C., Xing, Z., & Du, K. (2014). Vertical distribution of CO_2 in the atmospheric boundary layer: Characteristics and impact of meteorological variables. *Atmospheric Environment, 91*, 110–117. https://doi.org/10.1016/j.atmosenv.2014.03.067

Liou, K. N. (2002). *An introduction to atmospheric radiation* (2nd ed.). Academic Press.

Liu, Y., Wang, J., Yao, L., Chen, X., Cai, Z., Yang, D., Yin, Z., Gu, S., Tian, L., Lu, N., & Lyu, D. (2018). The TanSat mission: preliminary global observations. *Science Bulletin, 63*(18), 1200–1207. https://doi.org/10.1016/j.scib.2018.08.004

Liu, L., Huang, Y., Gyakum, J. R., Turner, D. D., & Gero, P. J. (2022). Trends in downwelling longwave radiance over the Southern Great Plains. *Journal of Geophysical Research: Atmospheres, 127*, e2021JD035949. https://doi.org/10.1029/2021JD035949

Liu, L., Bliankinshtein, N., Huang, Y., Gyakum, J. R., Gabriel, P. M., Xu, S., & Wolde, M. (2024). Radiative closure tests of collocated hyperspectral microwave and infrared radiometers. *Atmospheric Measurement Techniques, 17*, 2219–2233. https://doi.org/10.5194/amt-17-2219-2024

Lu, S., Wang, J., Wang, Y., & Yan, J. (2018). Analysis on the variations of atmospheric CO_2 concentrations along the urban–rural gradients of Chinese cities based on the OCO-2 XCO_2 data. *International Journal of Remote Sensing, 39*(12), 4194–4213. https://doi.org/10.1080/01431161.2017.1415482

Maahn, M., Turner, D. D., Löhnert, U., Posselt, D. J., Ebell, K., Mace, G. G., & Comstock, J. M. (2020). Optimal Estimation Retrievals and Their Uncertainties: What Every Atmospheric Scientist Should Know. *Bulletin of the American Meteorological Society, 101*(9), E1512–E1523. https://doi.org/10.1175/BAMS-D-19-0027.1

Markowski, P., & Richardson, Y. (2010). *Mesoscale meteorology in midlatitudes*. Wiley-Blackwell.

Mitchell, J. F. (1989). The "greenhouse" effect and climate change. *Reviews of Geophysics, 27*(1), 115–139.

Mitchell, L. E., Crosmana, E. T., Jacquesa, A. A., Fasolia, B., Leclair-Marzolfa, L., Horela, J., Bowlingb, D. R., Ehleringerb, J. R., & Lin, J. C. (2018). Monitoring of greenhouse gases and pollutants across an urban area using a light-rail public transit platform. *Atmospheric Environment, 187*, 9–23. https://doi.org/10.1016/j.atmosenv.2018.05.044

Mottungan, K., Brocchi, V., Roychoudhury, C., Gaubert, B., Tang, W., Mirrezaei, M. A., McKinnon, J., Guo1, Y., & Arellano, A. F. (2024). *Local and Regional Enhancements of CH_4, CO, and CO_2 Inferred from TCCON Column Measurements*. Preprint EGUsphere. https://doi.org/10.5194/egusphere-2024-705

National Oceanic and Atmospheric Administration. (n.d.). *Atmospheric Boundary Layer*. National Weather Service. https://forecast.weather.gov/glossary.php?word=boundary%20layer#:~:text=Atmospheric%20Boundary%20Layer&text=For%20the%20earth%2C%20this%20layer,friction%20with%20the%20earth's%20surface

O'Dell, C. W., Connor, B., Bösch, H., O'Brien, D., Frankenberg, C., Castano, R., Christi, M., Eldering, D., Fisher, B., Gunson, M., McDuffie, J., Miller, C. E., Natraj, V., Oyafuso, F., Polonsky, I., Smyth, M., Taylor, T., Toon, G. C., Wennberg, P. O., & Wunch, D. (2012). The ACOS CO_2 retrieval algorithm – Part 1: Description and validation against synthetic observations. *Atmospheric Measurement Techniques, 5*, 99–121. https://doi.org/10.5194/amt-5-99-2012

Ohyama, H., Frey, M. M., Morino, I., Shiomi, K., Nishihashi, M., Miyauchi, T., Yamada, H., Saito, M., Wakasa, M., Blumenstock, T., & Hase, F. (2023). Anthropogenic CO_2 emission estimates in the Tokyo metropolitan area from ground-based CO_2 column observations. *Atmospheric Chemistry and Physics, 23*, 15097–15119. https://doi.org/10.5194/acp-23-15097-2023

Park, H., Jeong, S., Park, H., Labzovskii, L. D., & Bowman, K. W. (2021). An assessment of emission characteristics of Northern Hemisphere cities using spaceborne observations of CO_2, CO, and NO_2. *Remote Sensing of Environment, 254*, 112246. https://doi.org/10.1016/j.rse.2020.112246

Park, C., Jeong, S., Park, H., Sim, S., Hong, J., & Oh, E. (2022). Comprehensive assessment of vertical variations in urban atmospheric CO_2 concentrations by using tall tower measurement and an atmospheric transport model. *Urban Climate, 45*, 101283. https://doi.org/10.1016/j.uclim.2022.101283

Parker, H. A., Laughner, J. L., Toon, G. C., Wunch, D., Roehl, C. M., Iraci, L. T., Podolske, J. R., McKain, K., Baier, B. C., & Wennberg, P. O. (2023). Inferring the vertical distribution of CO and CO_2 from TCCON total column values using the TARDISS algorithm. *Atmospheric Measurement Techniques, 16*, 2601–2625. https://doi.org/10.5194/amt-16-2601-2023

Picarro, Inc. (n.d.). *G2201-i Analyzer Datasheet*. https://www.picarro.com/environmental/support/library/documents/g2201i_analyzer_datasheet

Pörtner, H.-O., D.C. Roberts, H. Adams, I. Adelekan, C. Adler, R. Adrian, P. Aldunce, E. Ali, R. Ara Begum, B. Bednar-Friedl, R. Bezner Kerr, R. Biesbroek, J. Birkmann, K. Bowen, M.A. Caretta, J. Carnicer, E. Castellanos, T.S. Cheong, W. Chow … Z. Zaiton Ibrahim. (2022). Technical Summary. In H.-O. Pörtner, D.C. Roberts, E.S. Poloczanska, K. Mintenbeck, M. Tignor, A. Alegría, M. Craig, S. Langsdorf, S. Löschke, V. Möller & A. Okem (Eds.), *Climate Change 2022: Impacts, Adaptation and Vulnerability. Contribution of Working Group II to the Sixth Assessment Report of the Intergovernmental Panel on Climate Change* (pp. 37–118). Cambridge University Press. https://doi.org/10.1017/9781009325844.002

Roche, S., Strong, K., Wunch, D., Mendonca, J., Sweeney, C., Baier, B., Biraud, S.C., Laughner, J.L., Toon, G.C., & Connor, B.J. (2021). Retrieval of atmospheric CO_2 vertical profiles from ground-based near-infrared spectra. *Atmospheric Measurement Techniques, 14*, 3087–3118. https://doi.org/10.5194/amt-14-3087-2021

Rodgers, C. D. (2000). *Inverse Methods for Atmospheric Sounding: Theory and Practice*. World Scientific. https://doi.org/10.1142/3171

Seo, J., Choi, H., & Oh, Y. (2022). Potential of AOD Retrieval Using Atmospheric Emitted Radiance Interferometer (AERI). *Remote Sensing, 14*(2), 407. https://doi.org/10.3390/rs14020407

Shan, C., Wang, W., Xie, Y., Wu, P., Xu, J., Zeng, X., Zha, L., Zhu, Q., Sun, Y., Hu, Q., Cheng Liu, C., & Jones, N. (2022). Observations of atmospheric CO_2 and CO based on in-situ and ground-based remote sensing measurements at Hefei site, China. *Science of the Total Environment, 851*, 158188. https://doi.org/10.1016/j.scitotenv.2022.158188

Smith, E.N., Greene, B.R., Bell, T.M., Blumberg, W. G., Wakefield, R., Reif, D., Niu, Q., Wang, Q., & Turner, D. D. (2021). Evaluation and Applications of Multi-Instrument Boundary-Layer Thermodynamic Retrievals. *Boundary-Layer Meteorology, 181*, 95–123. https://doi.org/10.1007/s10546-021-00640-2

Turner, D. D., Knuteson, R. O., Revercomb, H. E., Lo, C., & Dedecker, R. G. (2006). Noise Reduction of Atmospheric Emitted Radiance Interferometer (AERI) Observations Using Principal Component Analysis. *Journal of Atmospheric and Oceanic Technology, 23*(9), 1223–1238. https://doi.org/10.1175/JTECH1906.1

Turner, D. D., & Blumberg, W. G. (2018). Improvements to the AERIoe thermodynamic profile retrieval algorithm. *IEEE Journal of Selected Topics in Applied Earth Observations and Remote Sensing, 12*(5), 1339–1354. https://doi.org/10.1109/JSTARS.2018.2874968

United Nations. (n.d.). *For a livable climate: Net-zero commitments must be backed by credible action*. https://www.un.org/en/climatechange/net-zero-coalition

Venturi, S., Tassi, F., Cabassi, J., Gioli, B., Baronti, S., Vaselli, O., Caponi, C., Vagnoli, C., Picchi, G., Zaldei, A., Magi, F., Miglietta, F., & Capecchiacci, F. (2020). Seasonal and diurnal variations of greenhouse gases in Florence (Italy): Inferring sources and sinks from carbon isotopic ratios. *Science of The Total Environment, 698*, 134245. https://doi.org/10.1016/j.scitotenv.2019.134245

Wu, Z., Pang, X., Xing, B., Zhao, G., Sun, S., Yuan, K., Lu, Y., Sun, Q., Shang, Q., Lu, Y., Lyu, Y., & Chen, D. (2023). Three-dimensional spatiotemporal variability of CO_2 in suburban and urban areas of Shaoxing City in the Yangtze River Delta, China. *Science of The Total Environment, 881*, 163501. https://doi.org/10.1016/j.scitotenv.2023.163501

Wunch, D., Toon, G. C., Blavier, J. F. L., Washenfelder, R. A., Notholt, J., Connor, B. J., Griffith, D. W., Sherlock, V., & Wennberg, P. O. (2011). The total carbon column observing network. *Philosophical Transactions of the Royal Society of London A: Mathematical, Physical and Engineering Sciences, 369*(1943), 2087–2112. https://doi.org/10.1098/rsta.2010.0240

Wunch, D., Wennberg, P. O., Osterman, G., Fisher, B., Naylor, B., Roehl, C. M., O'Dell, C., Mandrake, L., Viatte, C., Kiel, M., Griffith, D. W. T., Deutscher, N. M., Velazco, V. A., Notholt, J., Warneke, T., Petri, C., De Maziere, M., Sha, M. K., Sussmann, R., … Eldering, A. (2017). Comparisons of the Orbiting Carbon Observatory-2 (OCO-2) XCO_2 measurements with TCCON. *Atmospheric Measurement Techniques, 10*, 2209–2238. https://doi.org/10.5194/amt10-2209-2017

Yang, H., Feng, G., Xiang, R., Xu, Y., Qin, Y., & Li, S. (2020). Spatio-Temporal Validation of AIRS CO2 Observations Using GAW, HIPPO and TCCON. *Remote Sensing, 12*, 3583. https://doi.org/10.3390/rs12213583

Xia, L., Zhang, G., Liu, L., Zhan, M., Feng, M., Kong, P., & Dai, Z. (2022). Observation of atmospheric CO_2 and CO in a low-carbon pilot city: insight into CO_2 sources and regional transport. *Atmospheric Pollution Research, 13*, 101585. https://doi.org/10.1016/j.apr.2022.101585

Xie, F., Ren, T., Zhao, Z., & Zhao, C. (2023). A machine learning based line-by-line absorption coefficient model for the application of atmospheric carbon dioxide remote sensing. *Journal of Quantitative Spectroscopy and Radiative Transfer, 296*, 108441. https://doi.org/10.1016/j.jqsrt.2022.108441

Appendix A. Data and Codes

The data used for both synthetic experiments and retrieval utilizing real measurements, as well as the programs necessary to run the retrieval are located in the following link: https://github.com/bghirardi/Codes_Manuscript

In the "Analytical Jacobian Inputs" folder, you will find the necessary input files for LBLRTM to run the Analytical Jacobian calculation.

In the "Data" folder, you will find a file with the data used for the synthetic experiments ("era5_climatology") and one for the real measurements ("combined_profile").

In the "Main Functions" folder, you will find the MATLAB functions that are necessary to run the following codes.

In the "Noise AERI" folder, you will find the code to get the necessary AERI noise. This step needs to be taken before the retrieval is attempted, since the noise obtained from this code is necessary for the retrieval.

In the "Synthetic Experiments" folder, you will find the codes for the retrieval of the different cases presented in sections 4.1 and 4.2 of the synthetic experiment results.

In the "Real Measurements" folder, you will find the code for the retrieval using real AERI and atmospheric measurement data.

Finally, in the "Pos-retrieval" folder, you will find the codes to do the analysis of the retrieval results. These codes can be used for both synthetic and real experiments, the only difference being the input provided. These codes also generate the figures shown in the work.